J. Fluid Mech. (2009), *vol.* 636, *pp.* 177–216.
doi:10.1017/S002211200900768X

A high-order moment approach for capturing non-equilibrium phenomena in the transition regime

XIAO-JUN GU† AND DAVID R. EMERSON

Computational Science and Engineering Department, STFC Daresbury Laboratory, Warrington WA4 4AD, UK

(Received 10 October 2008; revised 13 April 2009; accepted 14 April 2009)

The method of moments is employed to extend the validity of continuum-hydrodynamic models into the transition-flow regime. An evaluation of the regularized 13 moment equations for two confined flow problems, planar Couette and Poiseuille flows, indicates some important limitations. For planar Couette flow at a Knudsen number of 0.25, they fail to reproduce the Knudsen-layer velocity profile observed using a direct simulation Monte Carlo approach, and the higher-order moments are not captured particularly well. Moreover, for Poiseuille flow, this system of equations creates a large slip velocity leading to significant overprediction of the mass flow rate for Knudsen numbers above 0.4. To overcome some of these difficulties, the theory of regularized moment equations is extended to 26 moment equations. This new set of equations highlights the importance of both gradient and non-gradient transport mechanisms and is shown to overcome many of the limitations observed in the regularized 13 moment equations. In particular, for planar Couette flow, they can successfully capture the observed Knudsen-layer velocity profile well into the transition regime. Moreover, this new set of equations can correctly predict the Knudsen layer, the velocity profile and the mass flow rate of pressure-driven Poiseuille flow for Knudsen numbers up to 1.0 and captures the bimodal temperature profile in force-driven Poiseuille flow. Above this value, the 26 moment equations are not able to accurately capture the velocity profile in the centre of the channel. However, they are able to capture the basic trends and successfully predict a Knudsen minimum at the correct value of the Knudsen number.

1. Introduction

The behaviour of a rarefied gas can readily be described by kinetic theory and the Boltzmann equation (Cercignani 1988). However, the theoretical treatment of the Boltzmann equation for practical applications remains formidable due to the complicated structure of the collision term and its high dimensionality. In recent years, there has been some advancement in the numerical simulation of several rarefied gasdynamics problems through solving the linearized Boltzmann equation directly, but these are often for simplified test cases, such as Kramers's problem (Siewert 2003), planar Couette flow (Sone, Takata & Ohwada 1990), cylindrical Couette flow (Aoki *et al.* 2003) and channel/Poiseuille flows involving small pressure

† Email address for correspondence: xiaojun.gu@stfc.ac.uk

and temperature gradients (Ohwada, Sone & Aoki 1989; Sharipov 1999). The direct simulation Monte Carlo (DSMC) method (Bird 1994) is an excellent alternative approach for solving high-speed rarefied gas flows, but the computational cost for low-speed flows in the slip- and transition-flow regime is too high for anything but very simplified problems. The recently developed lattice Boltzmann method (LBM) is constructed from simplified kinetic models that incorporate the essential physics of microscopic processes so that the macroscopic-averaged property obeys the desired macroscopic equations (Chen & Doolen 1998; Succi 2001). Unlike the solution of the Boltzmann equation, the LBM utilizes a minimal set of velocities in phase space so that the averaging process is greatly simplified. However, additional efforts are required when the conventional LBM is used to simulate gas flows under rarefied conditions (Chikatamarla, Ansumali & Karlin 2006; Zhang *et al.* 2007). The ability of the LBM to capture non-equilibrium phenomena in rarefied gas flows largely depends on the lattice model (Shan, Yuan & Chen 2006). For many years, alternative macroscopic modelling and simulation strategies have been developed (Chapman & Cowling 1970; Muller & Ruggeri 1993; Levermore 1996; Xu 2001; Shen, Fan & Xie 2003; Sun & Boyd 2004; Baker & Hadjiconstantinou 2005; Struchtrup 2005). However, with the advent of micro-electro-mechanical systems (MEMS) (Harley *et al.* 1995; Gad-el-Hak 1999; Reese, Gallis & Lockerby 2003), there has been a renewed impetus in the development of new and efficient approaches for modelling low-speed slip and transitional flows that can capture non-intuitive phenomena, such as Knudsen layers, and provide an accurate description of a gas that is not too far from thermodynamic equilibrium.

A macroscopic or hydrodynamic model of a dilute gas can be built up from its microscopic expression – the Boltzmann equation. The conventional hydrodynamic model of a gas is the Navier–Stokes–Fourier (NSF) equations, which govern the first five lowest moments of the molecular distribution function f: density, momentum and energy. The constitutive models for stresses and heat fluxes in the momentum and energy equations can be related to hydrodynamic quantities by a Chapman–Enskog (CE) expansion of the molecular distribution function in powers of the Knudsen number Kn (Chapman & Cowling 1970). The Knudsen number, which is the ratio of the mean free path of the gas molecules, λ, to a characteristic length scale, measures the degree of non-equilibrium of the gas. When the value of Kn is less than 0.1, the NSF equations, in association with velocity-slip and temperature-jump wall-boundary conditions (WBCs), can predict the velocity profile in a micro-channel fairly accurately (Gad-el-Hak 1999). The first-order CE expansion is consistent with the 'gradient transport mechanism' (GTM) for flow velocity u_i and temperature T in continuum mechanics, i.e. the Navier–Stokes equations and Fourier's law. As the value of Kn increases, because of either low-pressure or low-density conditions, or the size of a typical dimension of a device decreases, the gradient transport model no longer remains accurate due to an insufficient number of molecular collisions occurring to reach an equilibrium state. The NSF approach can be improved by introducing higher-order terms through a CE expansion of the molecular distribution function. The series can then be truncated at any power of Knudsen number, but if the power series in Kn is continued, the approach leads to the Burnett (second-order) (Chapman & Cowling 1970) or super-Burnett (third-order) equations (Shavaliyev 1993). However, Grad (1963) has argued that no matter how high the expansion order is, the resulting system will only describe flows that are already very close to the continuum solution. Recently, Karlin & Gorban (2002) have pointed out that the Burnett equations violate the underlying physics behind the Boltzmann equation, and

the super-Burnett approximation does not improve the situation. This phenomenon is known as 'Bobylev's instability' (Bobylev 1982). However, Uribe, Velasco & García-Colín (2000) have argued that the Burnett equations are valid when the Knudsen number is small and that the hydrodynamic instability only arises when the Burnett equations are applied beyond their range of validity. A review of the problems and successes of Burnett hydrodynamics has been given by García-Colín, Velaso & Uribe (2008).

Grad (1949*b*) proposed an approximate solution procedure for the Boltzmann equation via the moment method. In the method of moments, a set of N moments $\rho_{i_1 i_2 \ldots\ldots i_N}$ are defined to describe the state of the gas by

$$\rho_{i_1 i_2 \ldots i_N} = \int c_{i_1} c_{i_2} \ldots c_{i_N} f \, \mathrm{d}\boldsymbol{\xi}, \tag{1}$$

where $\boldsymbol{\xi}$ represents the molecule's velocity and $c_i (= \xi_i - u_i)$ is the intrinsic or peculiar velocity. Grad (1949*b*) expanded f in Hermite polynomials, the coefficients of which are linear combinations of the moments of the molecular distribution function. An infinite set of Hermite coefficients is equivalent to the molecular distribution function itself, and no kinetic information is lost in such a system. In practice, the molecular distribution function has to be truncated, and the specific problem to be addressed will determine the order of the truncation. It is expected that as Kn increases, the order of the truncated Hermite polynomials would increase to provide an accurate description of the flow conditions. By choosing a sufficient number of Hermite coefficients, a general solution of the Boltzmann equation can be approximated. The governing equations of the moments involved in the Hermite coefficients can be derived from the Boltzmann equation. However, the set of equations are not closed, since the fluxes and the collision terms are unknown. The truncated distribution function is used to calculate the collision terms and higher moments in the fluxes as functions of the chosen moments to close the equation set. All the moments included in the truncated distribution function construct the 'Grad moment manifold' (GMM). These moments relax to the equilibrium state at a rate governed by their corresponding governing equations. The remaining higher moments outside the GMM, as calculated from the truncated distribution function, approach the GMM (not the equilibrium state) at a fast finite rate and then relax to the equilibrium state along with the GMM (Gorban, Karlin & Zinovyev 2004). In this sense, the moments outside the GMM are referred to as 'fast' moments, and those in the GMM are 'slow' moments (Gorban *et al.* 2004). However, it should be noted that the overall relaxation time for the moments both inside and outside the GMM to relax to the equilibrium state is of the same order.

In his seminal paper, Grad (1949*b*) truncated the distribution function at the third order in Hermite polynomials, which includes the five lowest moments of the collision invariants, stresses and heat fluxes. The governing equations of stresses and heat fluxes were derived from the Boltzmann equation in addition to the conservation laws for mass, momentum and energy. This governing set of 13 moment equations essentially constitutes an 'extended thermodynamic' or 'extended hydrodynamic' model which can describe flows that depart from local equilibrium. In the original set of 13 moment equations, all the higher moments outside the GMM are not allowed to deviate from the GMM. In other words, they approach the GMM at an infinite rate, which results in Grad's well-known 13 moment equations (G13). Karlin *et al.* (1998) treated the truncated Hermite polynomial distribution function as a pseudo-equilibrium distribution, instead of the Maxwellian, and applied a CE expansion to

allow some of the higher moments outside the GMM to approach this manifold with a faster but finite rate. However, they only considered the linearized Boltzmann equation and did not compute the various transport coefficients. More recently, Struchtrup & Torrilhon (2003) and Struchtrup (2005) obtained a regularized set of G13 equations by applying a CE-like expansion and an order-of-magnitude approach to the governing equations of the moments higher than second order. The constitutive models established for the third and higher moments were then used to regularize the 13 moment equations (R13). An alternative approach has been proposed by Jin & Slemrod (2001) who used a visco-elastic regularization procedure to develop a relaxed Burnett system through a relaxation of the pressure deviator and heat flux. This leads to a stable set of 13 governing equations that are weakly parabolic, and a detailed comparison between the R13 and the regularization of Jin & Slemrod (2001) has been performed by Struchtrup (2005). In the present study, the distribution function is truncated at the fourth order in Hermite polynomials, and a set of 26 moment equations are employed, which are regularized by the procedure used by Struchtrup & Torrilhon (2003) for the 13 moment equations.

The moment method is well known in kinetic theory and provides an alternative solution procedure to the Boltzmann equation (Kogan 1969). Previous studies by Reitebuch & Weiss (1999) and Marques & Kremer (2001) have used the 13 and 26 moment field equations, respectively, to investigate planar Couette flow. In addition, Struchtrup (2003) used the linearized form of Grad's 13 and 26 moment equations to study one-dimensional heat transfer in a micro-scale channel. However, moment methods are not well known in the field of continuum fluid dynamics. There are two important reasons why this could be the case. Firstly, moments higher than second-order have no clear intuitive physical meaning. Secondly, the original Grad's moment equations are a set of the first-order partial differential equations (PDEs) with hyperbolic characteristics, and the regularized moment equations are a mixed system of the first- and second-order PDEs. Traditionally these equations are used to study hyperbolic flows (Grad 1952, 1963; Torrilhon & Struchtrup 2004; Torrilhon 2006).

In the moment system, the higher moments provide the transport mechanism for the moments one order lower. For a gas flow close to the equilibrium state, a sufficient number of molecular isotropic collisions cause the flow to behave as a continuum so that the GTM prevails. As the value of Kn increases, a non-gradient transport mechanism (NGTM) occurs in addition to the GTM. In fact, both the GTM and the NGTM coexist in the transition regime. In this paper, the moments are explicitly decomposed into their GTM and NGTM components, as proposed by Gu & Emerson (2007) in their study of the R13 equations. As the value of the gradient transport component of a moment can be calculated from the value of the relevant moment one order lower, the governing equations for the non-gradient components of the moments are readily obtained from the moment equations. As a result, a system of second-order PDEs can be constructed with characteristics determined by the flow conditions. Developing unique boundary conditions is quite challenging: a previous study by Liu & Rincon (2004) used the minimal principle to minimize entropy production, whereas Gu & Emerson (2007) obtained a set of WBCs for the R13 equations using Maxwell's kinetic WBC and DSMC data. However, Torrilhon & Struchtrup (2008) found that Gu & Emerson (2007) had over-subscribed the boundary conditions for the R13 equations, which caused irregularities in the shear stress and temperature profiles near the wall. In the present study, this issue is resolved by using boundary conditions equivalent to those of Torrilhon & Struchtrup (2008).

The purpose of this paper is to bridge kinetic theory and conventional fluid dynamics in the transition regime. In the next section, the process of extending the moment equation set from 5 to 26 moments is described following the basis of the GMM extension. Both the GTM and the NGTM are emphasized. The WBCs for the system are presented in § 3. A moment realizability criterion and H-theorem are briefly described in § 4 and provide a guide to ensuring that the numerical solutions are physical. In § 5, the moments are decomposed into their GTM and NGTM components. The governing equations for the non-gradient components are obtained from the 26 moment equations, and the numerical procedure for solving the newly derived equations are briefly discussed. Planar Couette flow and Poiseuille flow are then studied in § 6 for Kn around unity. The computed results from the moment equations are compared with either DSMC data or solutions of the linearized Boltzmann equation (Ohwada *et al.* 1989). Concluding remarks are presented in § 7.

2. Extended thermodynamic governing equations

2.1. *Conventional hydrodynamic model – the NSF equations*

The traditional hydrodynamic quantities of density ρ, velocity u_i and temperature T correspond to the first five lowest order moments of the molecular distribution function. The governing equations of these hydrodynamic quantities for a dilute gas can be obtained from the Boltzmann equation and represent mass, momentum and energy conservation laws, respectively (Struchtrup 2005):

$$\frac{\partial \rho}{\partial t} + \frac{\partial \rho u_i}{\partial x_i} = 0, \tag{2}$$

$$\frac{\partial \rho\, u_i}{\partial t} + \frac{\partial \rho\, u_i u_j}{\partial x_j} + \frac{\partial \sigma_{ij}}{\partial x_j} = -\frac{\partial p}{\partial x_i} + \rho a_i \tag{3}$$

and

$$\frac{\partial \rho T}{\partial t} + \frac{\partial \rho u_i T}{\partial x_i} + \frac{2}{3R}\frac{\partial q_i}{\partial x_i} = -\frac{2}{3R}\left(p\frac{\partial u_i}{\partial x_i} + \sigma_{ij}\frac{\partial u_j}{\partial x_i}\right), \tag{4}$$

where t and x_i are temporal and spatial coordinates, respectively, and any suffix i, j, k represents the usual summation convention. The external acceleration is denoted by a_i and the pressure p is related to the temperature and density by the ideal gas law $p = \rho RT$, where R is the specific gas constant. However, the stress term σ_{ij} and heat flux term q_i given in (3) and (4) are unknown. The classical way to close this set of equations is through a CE expansion of the molecular distribution function in terms of Kn around the Maxwellian, which is first order in Hermite polynomials. The zeroth-order CE expansion yields the Euler equations, and the first-order approximation of σ_{ij} and q_i, for Maxwell molecules, gives (Chapman & Cowling 1970; Struchtrup 2005)

$$\sigma_{ij}^G = -2\mu\frac{\partial u_{\langle i}}{\partial x_{j\rangle}} \text{ and } q_i^G = -\frac{15}{4}R\mu\frac{\partial T}{\partial x_i}, \tag{5}$$

in which μ is the viscosity and the angular brackets denote the traceless part of a symmetric tensor. Equation (5) expresses an import transport mechanism for u_i and T, the GTM, and the superscript G is used to emphasize the importance of this mechanism. If we let

$$\sigma_{ij} = \sigma_{ij}^G \text{ and } q_i = q_i^G \tag{6}$$

and insert (5) and (6) into (3) and (4), the result is the traditional hydrodynamic equations, i.e. the NSF equations. In the NSF system, the moments included in the GMM are $\{\rho,\ u_i,\ T\}$. This is an equilibrium manifold, which is a subset in any extended GMM. The CE expansion allows the higher moments σ_{ij} and q_i outside the manifold to deviate from the GMM. The second-order CE expansion adds the NGTM components to σ_{ij} and q_i and results in the Burnett equations.

2.2. *An extended hydrodynamic model – the R13 equations*

As the value of Kn increases, more moments need to be included in the GMM to accurately describe any non-equilibrium phenomenon. Grad (1949*b*) truncated the distribution function to the incomplete third order in Hermite polynomials (f_{G13}) and extended the GMM from $\{\rho,\ u_i,\ T\}$ to $\{\rho,\ u_i,\ T,\ \sigma_{ij},\ q_i\}$. Grad was one of the pioneers to introduce σ_{ij} and q_i as extended variables and derived a set of governing equations for them from the Boltzmann equation. For Maxwell molecules, the stress and heat flux equations are (Struchtrup 2005)

$$\frac{\partial \sigma_{ij}}{\partial t}+\frac{\partial u_k\sigma_{ij}}{\partial x_k}+\frac{\partial m_{ijk}}{\partial x_k}=-\frac{p}{\mu}\sigma_{ij}-2p\frac{\partial u_{\langle i}}{\partial x_{j\rangle}}+\Sigma_{ij} \tag{7}$$

and

$$\frac{\partial q_i}{\partial t}+\frac{\partial u_j q_i}{\partial x_j}+\frac{1}{2}\frac{\partial R_{ij}}{\partial x_j}=-\frac{2}{3}\frac{p}{\mu}q_i-\frac{5}{2}pR\frac{\partial T}{\partial x_i}+Q_i, \tag{8}$$

in which

$$\Sigma_{ij}=-\frac{4}{5}\frac{\partial q_{\langle i}}{\partial x_{j\rangle}}-2\sigma_{k\langle i}\frac{\partial u_{j\rangle}}{\partial x_k} \tag{9}$$

and

$$\begin{aligned}Q_i=&-\frac{7\sigma_{ik}R}{2}\frac{\partial T}{\partial x_k}-RT\frac{\partial \sigma_{ik}}{\partial x_k}+\frac{\sigma_{ij}}{\rho}\left(\frac{\partial p}{\partial x_j}+\frac{\partial \sigma_{jk}}{\partial x_k}\right)\\&-\frac{2}{5}\left(\frac{7}{2}q_k\frac{\partial u_i}{\partial x_k}+q_k\frac{\partial u_k}{\partial x_i}+q_i\frac{\partial u_k}{\partial x_k}\right)-\frac{1}{6}\frac{\partial \Delta}{\partial x_i}-m_{ijk}\frac{\partial u_j}{\partial x_k}.\end{aligned} \tag{10}$$

Here, m_{ijk}, R_{ij} and Δ represent the difference between the true value of the higher moments ($\rho_{\langle ijk\rangle}$, $\rho_{\langle ij\rangle rr}$ and ρ_{rrss}) and their approximated value with f_{G13}, respectively (Struchtrup & Torrilhon 2003), i.e.

$$\left.\begin{aligned}m_{ijk}&=\rho_{\langle ijk\rangle}-\rho_{\langle ijk\rangle|f_{G13}}=\rho_{\langle ijk\rangle},\\R_{ij}&=\rho_{\langle ij\rangle rr}-\rho_{\langle ij\rangle rr|f_{G13}}=\rho_{\langle ij\rangle rr}-7RT\sigma_{ij},\\\Delta&=\rho_{rrss}-\rho_{rrss\,|f_{G13}}=\rho_{rrss}-15pRT.\end{aligned}\right\} \tag{11}$$

In Grad's original method, such deviations were omitted, so that $m_{ijk}=R_{ij}=\Delta=0$. This results in the well-known G13 equations. To close the set of equations (2)–(4), (7) and (8), Struchtrup & Torrilhon (2003) and Struchtrup (2005) regularized the G13 equations and obtained the following closures:

$$m_{ijk}=-2\mu\frac{\partial(\sigma_{\langle ij}/\rho)}{\partial x_{k\rangle}}-\frac{8\mu}{5p}q_{\langle i}\frac{\partial u_j}{\partial x_{k\rangle}}, \tag{12}$$

$$\begin{aligned}R_{ij}=&-\frac{24}{5}\mu\frac{\partial(q_{\langle i}/\rho)}{\partial x_{j\rangle}}-\frac{24}{5}\frac{\mu}{p}q_{\langle i}\frac{\partial RT}{\partial x_{j\rangle}}-\frac{24}{7}\frac{\mu}{\rho}\\&\times\left(\sigma_{k\langle i}\frac{\partial u_{j\rangle}}{\partial x_k}+\sigma_{k\langle i}\frac{\partial u_k}{\partial x_{j\rangle}}-\frac{2}{3}\sigma_{ij}\frac{\partial u_k}{\partial x_k}\right)-\frac{4}{7}\frac{\sigma_{k\langle i}\sigma_{j\rangle k}}{\rho}\end{aligned} \tag{13}$$

and

$$\Delta = -\underline{12\mu\frac{\partial(q_k/\rho)}{\partial x_k}} - 20\frac{\mu}{p}q_k\frac{\partial RT}{\partial x_k} - 12\frac{\mu}{\rho}\sigma_{ij}\frac{\partial u_i}{\partial x_j} - \frac{\sigma_{ij}\sigma_{ij}}{\rho}. \tag{14}$$

Struchtrup (2005) denoted this set of 13 moment equations with the above closure as the R13 equations. The underlined terms on the right-hand sides of (12)–(14) provide the GTM for σ_{ij} and q_i and help to stabilize the R13 equations. It is convenient to explicitly describe the gradient transport components by

$$m^G_{ijk} = -2\mu\frac{\partial(\sigma_{\langle ij}/\rho)}{\partial x_{k\rangle}},\ R^G_{ij} = -\frac{24}{5}\mu\frac{\partial(q_{\langle i}/\rho)}{\partial x_{j\rangle}} \text{ and } \Delta^G = -12\mu\frac{\partial(q_k/\rho)}{\partial x_k}. \tag{15}$$

The rest of the terms in (12)–(14) represent the NGTM components of the corresponding moments. It is clear that the GTM not only exists for lower-rank moments, such as velocity and temperature, but also for high-rank moments, such as stress and heat flux.

2.3. *Extending the hydrodynamic model – the R26 equations*

In a recent study of planar Couette flow, Gu, Barber & Emerson (2007) and Gu & Emerson (2007) found that the R13 equations improved Grad's original closure significantly, but they were not able to capture the Knudsen-layer velocity profile accurately. Since (12) and (13) are constitutive relationships for m_{ijk} and $R_{ij,}$ they can only provide a mechanism to produce a boundary layer for the lower-order moments σ_{ij} and q_i but have no mechanism to produce their own boundary layer near the wall (Torrilhon & Structrup 2008). As the Knudsen layer is a linear superposition of many exponential layers (Struchtrup 2008), the R13 equations only resolve one such contribution. Mizzi *et al.* (2008) introduced m_{ijk} into the governing equations to alleviate this problem. In the present approach, the GTMs for m_{ijk} and R_{ij} near the wall are provided by extending the GMM from 13 to 26 moments, which includes the moments m_{ijk}, R_{ij} and Δ as extended hydrodynamic variables. The distribution function is truncated to the incomplete fourth order in Hermite polynomials (f_{G26}), and the GMM is extended from $\{\rho,\ u_i,\ T,\sigma_{ij},\ q_i\}$ to $\{\rho,\ u_i,\ T,\ \sigma_{ij},\ q_i,\ m_{ijk},\ R_{ij},\ \Delta\}$. From the Boltzmann equation, it is possible to obtain governing equations for m_{ijk}, R_{ij} and Δ for Maxwell molecules as follows (Struchtrup 2005):

$$\frac{\partial m_{ijk}}{\partial t} + \frac{\partial u_l m_{ijk}}{\partial x_l} + \frac{\partial \phi_{ijkl}}{\partial x_l} = -\frac{3}{2}\frac{p}{\mu}m_{ijk} - 3p\frac{\partial(\sigma_{\langle ij}/\rho)}{\partial x_{k\rangle}} + \mathfrak{M}_{ijk}, \tag{16}$$

$$\frac{\partial R_{ij}}{\partial t} + \frac{\partial u_k R_{ij}}{\partial x_k} + \frac{\partial \psi_{ijk}}{\partial x_k} = -\frac{7}{6}\frac{p}{\mu}R_{ij} - \frac{28}{5}p\frac{\partial(q_{\langle i}/\rho)}{\partial x_{j\rangle}} + \mathfrak{R}_{ij} \tag{17}$$

and

$$\frac{\partial \Delta}{\partial t} + \frac{\partial \Delta u_i}{\partial x_i} + \frac{\partial \Omega_i}{\partial x_i} = -\frac{2}{3}\frac{p}{\mu}\Delta - 8p\frac{\partial(q_i/\rho)}{\partial x_i} + \aleph, \tag{18}$$

in which

$$\mathfrak{M}_{ijk} = 3\frac{\sigma_{\langle ij}}{\rho}\frac{\partial \sigma_{k\rangle l}}{\partial x_l} - \frac{12}{5}q_{\langle i}\frac{\partial u_j}{\partial x_{k\rangle}} - 3m_{l\langle ij}\frac{\partial u_{k\rangle}}{\partial x_l} - \frac{3}{7}\frac{\partial R_{\langle ij}}{\partial x_{k\rangle}}, \tag{19}$$

$$\begin{aligned}\mathfrak{R}_{ij} = &-\frac{2}{3}\frac{p}{\mu}\frac{\sigma_{k\langle i}\sigma_{j\rangle k}}{\rho} - \frac{28}{5}q_{\langle i}\frac{\partial RT}{\partial x_{j\rangle}} + \frac{28}{5}\frac{q_{\langle i}}{\rho}\frac{\partial \sigma_{j\rangle k}}{\partial x_k} + \frac{14}{3}\frac{\sigma_{ij}}{\rho}\left(\frac{\partial q_k}{\partial x_k} + \sigma_{kl}\frac{\partial u_k}{\partial x_l}\right)\\ &- 4RT\left(\sigma_{k\langle i}\frac{\partial u_k}{\partial x_{j\rangle}} + \sigma_{k\langle i}\frac{\partial u_{j\rangle}}{\partial x_k} - \frac{2}{3}\sigma_{ij}\frac{\partial u_k}{\partial x_k}\right) - 2RT\frac{\partial m_{ijk}}{\partial x_k} - 9m_{ijk}\frac{\partial RT}{\partial x_k}\\ &- 2\phi_{ijkl}\frac{\partial u_k}{\partial x_l} + 2\frac{m_{ijk}}{\rho}\left(\frac{\partial p}{\partial x_k} + \frac{\partial \sigma_{kl}}{\partial x_l}\right) - \left(\frac{6}{7}R_{\langle ij}\frac{\partial u_{k\rangle}}{\partial x_k} + \frac{4}{5}R_{k\langle i}\frac{\partial u_k}{\partial x_{j\rangle}} + 2R_{k\langle i}\frac{\partial u_{j\rangle}}{\partial x_k}\right)\\ &- \frac{14}{15}\Delta\frac{\partial u_{\langle i}}{\partial x_{j\rangle}} - \frac{2}{5}\frac{\partial \Omega_{\langle i}}{\partial x_{j\rangle}}\end{aligned} \tag{20}$$

and

$$\aleph = -\frac{2}{3}\frac{p}{\mu}\frac{\sigma_{ij}\sigma_{ij}}{\rho} - 4(2RT\sigma_{ij} + R_{ij})\frac{\partial u_i}{\partial x_j} + 8\frac{q_i}{\rho}\frac{\partial \sigma_{ij}}{\partial x_j} - 20q_i\frac{\partial RT}{\partial x_i} - \frac{4}{3}\Delta\frac{\partial u_i}{\partial x_i}. \tag{21}$$

Here, ϕ_{ijkl}, ψ_{ijk} and Ω_i are the difference between the true value of the higher moments ($\rho_{\langle ijkl\rangle}$, $\rho_{rr\langle ijk\rangle}$ and ρ_{rrssi}) and their corresponding value approximated with f_{G26}, i.e.

$$\left.\begin{aligned}\phi_{ijkl} &= \rho_{\langle ijkl\rangle} - \rho_{\langle ijkl\rangle|f_{G26}} = \rho_{\langle ijkl\rangle},\\ \psi_{ijk} &= \rho_{rr\langle ijk\rangle} - \rho_{rr\langle ijk\rangle|f_{G26}} = \rho_{rr\langle ijk\rangle} - 9RTm_{ijk},\\ \Omega_i &= \rho_{rrssi} - \rho_{rrssi|f_{G26}} = \rho_{rrssi} - 28RTq_i.\end{aligned}\right\} \tag{22}$$

If deviations are not allowed for the higher moments away from the GMM, the above equations become a Grad-type 26 moment set of equations. In the present study, these equations are regularized following the procedure used by Struchtrup & Torrilhon (2003). The governing equations for ϕ_{ijkl}, ψ_{ijk} and Ω_i are derived from the Boltzmann equation, and a CE-like expansion (Struchtrup & Torrilhon 2003) is applied to them. However, when the nonlinear collision terms are included in these equations, care must be taken to ensure that the CE expansion only allows ϕ_{ijkl}, ψ_{ijk} and Ω_i to approach the GMM (not directly the equilibrium state) at a fast rate and then follow the GMM towards the equilibrium state, as detailed in appendix A. Combining (A8) and (A9), the 26 moment field equations are closed by

$$\phi_{ijkl} = \underline{-\frac{4\mu}{C_1}\frac{\partial(m_{\langle ijk}/\rho)}{\partial x_{l\rangle}}} + \phi^R_{ijkl}, \quad \psi_{ijk} = \underline{-\frac{27\mu}{7Y_1}\frac{\partial(R_{\langle ij}/\rho)}{\partial x_{k\rangle}}} + \psi^R_{ijk}$$
$$\text{and} \quad \Omega_i = \underline{-\frac{7\mu}{3}\frac{\partial(\Delta/\rho)}{\partial x_i}} + \Omega^R_i. \tag{23}$$

Here ϕ^R_{ijkl}, ψ^R_{ijk} and Ω^R_i are the remaining terms of ϕ_{ijkl}, ψ_{ijk} and Ω_i, respectively, and are expressed by

$$\phi^R_{ijkl} = -\frac{12}{C_1}\frac{\mu}{\rho}\sigma_{\langle ij}\frac{\partial u_k}{\partial x_{l\rangle}} + \frac{4\mu}{C_1 p\rho}m_{\langle ijk}\frac{\partial \sigma_{l\rangle m}}{\partial x_m} - \frac{12}{7}\frac{\mu R_{\langle ij}}{C_1 p}\frac{\partial u_k}{\partial x_{l\rangle}} - \frac{C_2}{C_1}\frac{\sigma_{\langle ij}\sigma_{kl\rangle}}{\rho}, \tag{24}$$

$$\begin{aligned}\psi^R_{ijk} = {} & -\frac{27}{7}\frac{\mu}{Y_1 p}(R_{\langle ij} + 7RT\sigma_{\langle ij})\frac{\partial RT}{\partial x_{k\rangle}} - \frac{108}{5Y_1}\frac{\mu}{\rho}q_{\langle i}\frac{\partial u_j}{\partial x_{k\rangle}} + \frac{27\mu}{7Y_1}\frac{R_{\langle ij}}{p\rho}\frac{\partial \sigma_{k\rangle m}}{\partial x_m} + \frac{6\mu}{Y_1 p}\frac{m_{ijk}}{\rho} \\ & \times\left(\frac{\partial q_m}{\partial x_m} + \sigma_{ml}\frac{\partial u_m}{\partial x_l}\right) - \frac{\mu}{Y_1\rho}\left(\frac{54}{7}m_{m\langle ij}\frac{\partial u_m}{\partial x_{k\rangle}} + 8m_{\langle ijk}\frac{\partial u_{m\rangle}}{\partial x_m} - 6m_{ijk}\frac{\partial u_m}{\partial x_m}\right) \\ & - \left(\frac{Y_2}{Y_1}\frac{\sigma_{\langle li}m_{jkl\rangle}}{\rho} + \frac{Y_3}{Y_1}\frac{q_{\langle i}\sigma_{jk\rangle}}{\rho}\right)\end{aligned} \tag{25}$$

and

$$\begin{aligned}\Omega^R_i = {} & -4\mu\frac{\partial(R_{ij}/\rho)}{\partial x_j} - \frac{56}{5}\frac{\mu}{\rho}\left(q_j\frac{\partial u_i}{\partial x_j} + q_j\frac{\partial u_j}{\partial x_i}\right) - 8\frac{\mu}{\rho}m_{ijk}\frac{\partial u_j}{\partial x_k} - 14\frac{\mu}{p}(2RT\sigma_{ij} + R_{ij}) \\ & \times\frac{\partial RT}{\partial x_j} + \frac{56}{3}\frac{\mu}{p}\frac{q_i}{\rho}\left(\frac{\partial q_j}{\partial x_j} + \sigma_{jk}\frac{\partial u_j}{\partial x_k}\right) + 4\frac{\mu}{p}\frac{R_{ij}}{\rho}\frac{\partial \sigma_{jk}}{\partial x_k} + \frac{7}{3}\frac{\mu}{p}\Delta\left(\frac{\partial \sigma_{ij}}{\rho\partial x_j} - 2\frac{\partial RT}{\partial x_i}\right) \\ & - \frac{2}{15}\left(\frac{5m_{ijk}\sigma_{jk} + 14q_j\sigma_{ij}}{\rho}\right),\end{aligned} \tag{26}$$

in which C_1, C_2, Y_1, Y_2 and Y_3 are collision term constants, and their values are given in appendix A. The underlined terms on the right-hand side of (23) provide the GTM for m_{ijk}, R_{ij} and Δ and play an important role in the region close to the wall. Again, the GTM can be explicitly expressed by

$$\phi^G_{ijkl} = -\frac{4\mu}{C_1}\frac{\partial(m_{\langle ijk}/\rho)}{\partial x_{l\rangle}}, \quad \psi^G_{ijk} = -\frac{27\mu}{7Y_1}\frac{\partial(R_{\langle ij}/\rho)}{\partial x_{k\rangle}} \quad \text{and} \quad \Omega^G_i = -\frac{7\mu}{3}\frac{\partial(\Delta/\rho)}{\partial x_i}. \tag{27}$$

Following the convention of Struchtrup (2005), the above closed set of 26 moment equations are denoted as the R26 equations, which is a mixed system of first- and second-order PDEs.

An alternative approach to close the moment equations is the order-of-magnitude method proposed by Struchtrup (2004, 2005). This method relates the importance of the moments to the Knudsen number and gives an order of accuracy to the moment equation system. Struchtrup (2004) showed that the NSF equations are first order in Kn; Grad's 13 moment system is of second order; and the R13 moment equations are of third order. Assigning the corresponding order to the moments in the R26 moment equations indicates that they are of fifth-order accuracy, as stated by Struchtrup (2005). Although the order of magnitude analysis may not be applicable in the Knudsen layer (Struchtrup 2008), it does provide valuable insight into the role of the moments and their governing equations.

3. Wall boundary conditions

To apply any of the foregoing models to flows in confined geometries, appropriate WBCs are required to determine a unique solution. One of the difficulties encountered in any investigation of WBCs is a limited understanding of the structure of surface layers of solid bodies and of the effective interaction potential of the gas molecules with the wall. A scattering kernel represents a fundamental concept in gas-surface interactions, by means of which other quantities should be defined (Cercignani 2000).

Gu & Emerson (2007) obtained a set of WBCs for the R13 moment equations based on Maxwell's kinetic wall boundary model (Maxwell 1879) and a fourth-order approximation of the molecular distribution function in Hermite polynomials. To construct WBCs for the R26 equations, a fifth-order approximation of the molecular distribution function, $f^{(5)}$, is required. With the Hermite polynomials and their coefficients listed in appendix B, it is expressed by

$$f^{(5)} = f_M\,(1+\varphi)\,, \tag{28}$$

in which

$$\begin{aligned}\varphi = \Bigg[&\frac{\sigma_{ij}c_ic_j}{2pRT} + \frac{c_iq_i}{pRT}\left(\frac{c^2}{5RT}-1\right) + \frac{m_{ijk}c_ic_jc_k}{6p(RT)^2} + \frac{R_{ij}c_ic_j}{4p(RT)^2}\left(\frac{c^2}{7RT}-1\right) + \frac{\Delta}{8pRT}\\ &\times\left(\frac{c^4}{15(RT)^2} - \frac{2c^2}{3RT} + 1\right) + \underline{\frac{\phi_{ijkl}c_ic_jc_kc_l}{24p\,(RT)^3} + \frac{\psi_{ijk}c_ic_jc_k}{12p\,(RT)^3}\left(\frac{c^2}{9RT}-1\right)}\\ &+ \underline{\frac{c_i\Omega_i}{40p(RT)^2}\left(\frac{c^4}{7(RT)^2} - \frac{2c^2}{RT} + 5\right)}\Bigg]\,,\end{aligned} \tag{29}$$

where $c^2 = c_kc_k$. It should be noted that the higher moments involved in the underlined terms in (29) are not part of the GMM so that $f^{(5)}$ is not a Grad-type distribution function but a regularized f_{G26} and is used to construct the WBCs to increase the accuracy near the wall.

Maxwell's kinetic boundary condition (Maxwell 1879) is a rather simple model, and it states that a fraction $(1-\alpha)$ of gas molecules will undergo 'specular' reflection, while the remaining fraction α will be 'diffusely' reflected with a Maxwellian distribution f_M^w at the temperature of the wall T_w. In a frame in which the coordinates are attached to the wall, with n_i the normal vector of the wall pointing towards the gas and τ_i the tangential vector of the wall, such that all molecules with $\xi_in_i<0$ are incident upon the wall and molecules with $\xi_in_i\geqslant 0$ are emitted by the wall, Maxwell's boundary condition can be expressed by (Struchtrup 2005)

$$f^w = \begin{cases} \alpha f_M^w + (1-\alpha)\,f(-\xi_in_i), & \xi_in_i\geqslant 0,\\ f(\xi_in_i), & \xi_in_i<0.\end{cases} \tag{30}$$

By definition, the value of any moment at the wall can be obtained from

$$\int_{\xi_in_i\geqslant 0} c_{i_1}c_{i_2}\ldots c_{i_n}\,f(\xi_in_i)\mathrm{d}\boldsymbol{\xi} = \int_{\xi_in_i\geqslant 0} c_{i_1}c_{i_2}\ldots c_{i_n}\left[\alpha f_M^w + (1-\alpha)\,f(-\xi_in_i)\right]\mathrm{d}\boldsymbol{\xi}. \tag{31}$$

Grad (1949*b*) considered the special case of $\alpha=0$ and concluded that only moments that are odd functions of c_in_i can be used to construct WBCs. Furthermore, Torrilhon & Struchtrup (2008) determined that only the moments representing fluxes can be used in the boundary conditions. This limits the choice of moments to $\boldsymbol{\psi} = (c_n, c_\tau c_n, c^2c_n, c_\tau^2c_n, c_n^3, c^2c_\tau c_n, c_\tau^3c_n, c_\tau c_n^3, c_\tau^3c_n^3, c_\tau^4c_n, c_n^5, c^4c_n)$, in which $c_n = c_in_i$ and $c_\tau = c_i\tau_i$. The details of the construction procedure of the WBCs for the R26 equations are the same as for the R13 equations (Gu & Emerson 2007; Torrilhon & Struchtrup 2008) and are not repeated here. The slip velocity parallel to the wall u_τ and temperature jump conditions are

$$u_\tau = -\frac{2-\alpha}{\alpha}\sqrt{\frac{\pi RT}{2}}\frac{\sigma_{n\tau}}{p_\alpha} - \underline{\frac{5m_{nn\tau}+2q_\tau}{10p_\alpha} + \frac{9\Omega_\tau + 70\psi_{nn\tau}}{2520p_\alpha RT}} \tag{32}$$

and

$$RT - RT_w = -\frac{2-\alpha}{\alpha}\sqrt{\frac{\pi RT}{2}}\frac{q_n}{2p_\alpha} - \underline{\frac{RT\sigma_{nn}}{4p_\alpha} + \frac{u_\tau^2}{4} - \frac{75R_{nn}+28\Delta}{840p_\alpha} + \frac{\phi_{nnnn}}{24p_\alpha}}, \tag{33}$$

where

$$p_\alpha = p + \frac{\sigma_{nn}}{2} - \frac{30R_{nn}+7\Delta}{840RT} - \frac{\phi_{nnnn}}{24RT}. \tag{34}$$

Here $\sigma_{nn} = \sigma_{ij}n_in_j$, $\sigma_{n\tau} = \sigma_{ij}n_i\tau_j$, $q_\tau = q_i\tau_i$, $m_{nn\tau} = m_{ijk}n_in_j\tau_k$, $m_{nnn} = m_{ijk}n_in_jn_k$, $R_{nn} = R_{ij}n_in_j$, $\psi_{nn\tau} = \psi_{ijk}n_in_j\tau_k$, $\Omega_\tau = \Omega_i\tau_i$ and $\phi_{nnnn} = \phi_{ijkl}n_in_jn_kn_l$ are the tangential and normal components of σ_{ij}, q_i, m_{ijk}, R_{ij}, ψ_{ijk}, Ω_i and ϕ_{ijkl} relative to the wall. It should be noted that the normal velocity at the wall $u_n = 0$, since there is no gas flow through the wall. Equations (32) and (33) are similar to the slip velocity and temperature jump conditions for the NSF equations (Cercignani 1988; Gad-el-Hak 1999) with the underlined terms on the right-hand side providing higher-order moment corrections. These underlined terms can be related to second- or higher-order velocity slip and temperature jump boundary conditions (Struchtrup & Torrilhon 2008). With a normalized slip velocity $\hat{u}_\tau = u_\tau/\sqrt{RT}$ and a normalized wall temperature $\hat{T}_w = T_w/T$ the rest of the WBCs are listed in appendix C. Equations (C1)–(C3) without the higher-order moments $\phi_{nn\tau\tau}$, ϕ_{nnnn}, $\psi_{nn\tau}$ and Ω_τ together with (32)–(34) are boundary conditions for the R13 equations, equivalent to those used by Torrilhon & Struchtrup (2008).

4. Moment realizability and H-theorem

Two important features of solutions to the Boltzmann equation is that the distribution function f is non-negative and that the solution must satisfy the H-theorem (Cercinani 1988). However, a solution obtained from the moment equations as an approximation to f may not satisfy these constraints. Struchtrup & Torrilhon (2007) have shown that the linearized R13 equations naturally fulfil the H-theorem. A full detailed analysis of the mathematical properties of the 26 moment equations is beyond the scope of the present study. However, this section will briefly explore the moment realizability criteria, and expressions for a generalized entropy and its flux will be given, which can be used to assess the validity of the numerical solution.

Instead of directly evaluating the value of the approximate distribution function $f^{(5)}$, the moment realizability criteria advocated by Levermore, Morokoff & Nadiga (1998) can be used to examine whether a numerical solution is realizable. From the elementary observation that if an approximate distribution function F is non-negative, then so is $\int \psi^2 F \mathrm{d}\boldsymbol{\xi}$ for any function $\psi = \psi(\boldsymbol{\xi})$, Levermore *et al.* (1998) derived a simple validity matrix $\boldsymbol{V}$ which includes all the densities and fluxes of the conservation laws. For these fluxes to be realizable, the eigenvalues of the validity matrix must be non-negative. With the approximate distribution function $f^{(5)}$ in (28), the elements of the matrix $\boldsymbol{V}$ can be expressed by

$$V_{ij} = \delta_{ij} + \frac{\sigma_{ij}}{p} - \frac{2}{3}\frac{q_iq_j}{p^2RT}\left(1 + \frac{\Delta}{6pRT}\right)^{-1}. \tag{35}$$

The quantity $\mathscr{H}$ defined by

$$\mathscr{H} = -\int f \ln f \, \mathrm{d}\boldsymbol{\xi} \tag{36}$$

plays a significant role in the theory of the Boltzmann equation (Cercignani 1988). For equilibrium flow, the value of $\mathscr{H}$ can be evaluated with the Maxwellian so that

$$\mathscr{H}^{eq} = -\int f^M \ln f^M \mathrm{d}\boldsymbol{\xi} = \frac{\rho}{R}\eta + \rho\, e_o, \tag{37}$$

where η is the thermodynamic or equilibrium entropy given by (Grad 1949*b*)

$$\eta = \frac{3}{2}R \ln\left(\frac{p}{\rho^{5/3}}\right) \tag{38}$$

and e_o is an entropy constant equal to $(3/2)(\ln 2\pi + 1)$. The quantity $\mathscr{H}$ can therefore be regarded as having properties of entropy (Grad 1949*b*; Cercignani 1988). Replacing f with $f^{(5)}$, an approximate value of $\mathscr{H}$ can be evaluated from

$$\mathscr{H} = -\int f^{(5)} \ln f^{(5)} \mathrm{d}\boldsymbol{\xi} = -\int f^M(1+\varphi)\ln[f^M(1+\varphi)]\mathrm{d}\boldsymbol{\xi}. \tag{39}$$

For flow not far from equilibrium, i.e. $|\varphi| < 1$, $\ln(1+\varphi)$ can be approximated as $\varphi - \varphi^2/2$, and (39) becomes

$$\mathscr{H} = \mathscr{H}^{eq} - \frac{1}{4p}\left(\frac{\sigma_{ij}\sigma_{ij}}{RT} + \frac{4q_iq_i}{5(RT)^2} + \frac{m_{ijk}m_{ijk}}{3(RT)^2} + \frac{R_{ij}R_{ij}}{14(RT)^3} + \frac{\Delta^2}{60(RT)^3} + \frac{\phi_{ijkl}\phi_{ijkl}}{12(RT)^3} + \frac{\psi_{ijk}\psi_{ijk}}{54(RT)^4} + \frac{\Omega_i\Omega_i}{140(RT)^4}\right). \tag{40}$$

Similarly, the flux of $\mathscr{H}$ in the direction of x_m, given by $J_m = -\int \xi_m f \ln f \,\mathrm{d}\boldsymbol{\xi}$, can be obtained from the distribution function $f^{(5)}$ as

$$J_m = u_m\mathscr{H} + \frac{q_m}{RT} - \frac{1}{2p}\left(\frac{4}{5}\frac{q_i\sigma_{mi}}{RT} + \frac{\sigma_{ij}m_{ijm}}{RT} + \frac{2q_iR_{im}}{5(RT)^2} + \frac{R_{ij}m_{ijm}}{7(RT)^2} + \frac{2\Delta q_m}{15(RT)^2}\right) - \frac{1}{2p}\left(\frac{R_{ij}\psi_{ijm}}{14(RT)^3} + \frac{\Omega_iR_{im}}{35(RT)^3} + \frac{23}{840}\frac{\Delta\Omega_m}{(RT)^3} + \frac{m_{ijk}\phi_{ijkm}}{3(RT)^2} + \frac{\psi_{ijk}\phi_{ijkm}}{27(RT)^3}\right). \tag{41}$$

In terms of $\mathscr{H}$ and J_m, the H-theorem of the Boltzmann equation can be expressed by (Cercignani 1988; Struchtrup 2005)

$$\frac{\partial\mathscr{H}}{\partial t} + \frac{\partial J_m}{\partial x_m} \geqslant 0. \tag{42}$$

This inequality is an essential feature of rarefied gasdynamics. It states the following: (i) for a homogenous system, the generalized entropy $\mathscr{H}$ never decreases with time; (ii) for a steady-state flow, the divergence of the flux of $\mathscr{H}$ is non-negative. The eigenvalues of matrix $\boldsymbol{V}$ and the inequality (42) can be readily evaluated numerically at any grid point to check whether a non-physical solution of the moment equations is obtained.

5. Numerical method

The moment equations have often been used to study shock structures in which the flows are hyperbolic in nature (Grad 1952; Jin, Pareshi & Slemrod 2002; Torrilhon & Struchtrup 2004). In the case of low-speed rarefied gas flow, such as those found in micro-devices, the system is parabolic or elliptic. Using a hyperbolic flow solver to solve elliptic flows is inefficient and expensive. In the present study, a primitive variable transformation is introduced in terms of the GTM and NGTM embedded

in the moment equation system. The moment equations are recast in a form in which conventional computational fluid dynamics techniques for low-speed flow can be employed.

5.1. *Primitive variable transformation*

In the theory of differential equations, variable substitutions or transformations are often used to show that certain classes of equations are equivalent to a standard form (Debnath 1997). Primitive variables of the governing equations for moments have been transformed during the development of the moment method. The full tensorial moments have been decomposed into their trace and traceless parts and further decomposed into their values on the GMM and their corresponding deviations (Grad 1949*b*; Truesdell & Muncaster 1980; Struchtrup 2005). These decompositions are local, and the resultant governing equations are always of a hyperbolic nature regardless of the flow conditions. This is inherited from the streaming part of the Boltzmann equation. However, the collisions at the microscopic level cause the macroscopic quantities of the flow to diffuse. As indicated in the previous section, the GTM exists for all the moments considered in the GMM up to 26 moments. The GTM of the low moments are embedded in the moments one order higher. For example, the diffusion of u_i is included in σ_{ij}, and the diffusion of σ_{ij} is included in m_{ijk}, and so on, as expressed by (5), (15) and (27). Equations (7), (8) and (16)–(18) can therefore be recast in terms of the GTM as

$$\frac{\partial \sigma_{ij}}{\partial t} + \frac{\partial u_k \sigma_{ij}}{\partial x_k} + \frac{\partial m_{ijk}}{\partial x_k} = -\underline{\frac{p}{\mu}\left(\sigma_{ij} - \sigma_{ij}^G\right)} + \Sigma_{ij}, \tag{43}$$

$$\frac{\partial q_i}{\partial t} + \frac{\partial u_j q_i}{\partial x_j} + \frac{1}{2}\frac{\partial R_{ij}}{\partial x_j} = -\underline{\frac{2}{3}\frac{p}{\mu}\left(q_i - q_i^G\right)} + Q_i, \tag{44}$$

$$\frac{\partial m_{ijk}}{\partial t} + \frac{\partial u_l m_{ijk}}{\partial x_l} + \frac{\partial \phi_{ijkl}}{\partial x_l} = -\underline{\frac{3}{2}\frac{p}{\mu}\left(m_{ijk} - m_{ijk}^G\right)} + \mathfrak{M}_{ijk}, \tag{45}$$

$$\frac{\partial R_{ij}}{\partial t} + \frac{\partial u_k R_{ij}}{\partial x_k} + \frac{\partial \psi_{ijk}}{\partial x_k} = -\underline{\frac{7}{6}\frac{p}{\mu}\left(R_{ij} - R_{ij}^G\right)} + \mathfrak{R}_{ij} \tag{46}$$

and

$$\frac{\partial \Delta}{\partial t} + \frac{\partial \Delta u_i}{\partial x_i} + \frac{\partial \Omega_i}{\partial x_i} = -\underline{\frac{2}{3}\frac{p}{\mu}\left(\Delta - \Delta^G\right)} + \aleph. \tag{47}$$

It is interesting to note that the above set of equations have a common feature in that these moments tend to relax towards the equilibrium state via the values which provide the gradient transport for the moments one order lower, as expressed by the underlined terms on the right-hand sides of (43)–(47). This phenomenon is clearly caused by the collisions between the molecules. To make full use of the physical aspect of this phenomenon for computation, the moments are decomposed into their GTM and NGTM components defined by

$$\sigma_{ij} = \sigma_{ij}^G + \rho g_{ij}, \quad q_i = q_i^G + \rho h_i, \quad m_{ijk} = m_{ijk}^G + \rho \omega_{ijk}, \quad R_{ij} = R_{ij}^G + \rho \gamma_{ij}$$
$$\text{and } \Delta = \Delta^G + \rho \chi, \tag{48}$$

where ρg_{ij}, ρh_i, $\rho \omega_{ijk}$, $\rho \gamma_{ij}$ and $\rho \chi$ are the NGTM components for σ_{ij}, q_i, m_{ijk}, R_{ij} and Δ, respectively. This decomposition, which was originally proposed by Gu & Emerson (2007) in their study of the R13 equations, is non-local and symmetric. This approach to the decomposition is analogous to the visco-elastic stress-splitting

technique used in non-Newtonian fluid modelling (Rajagopalan, Armstrong & Brown 1990; Guénette & Fortin 1995; Renardy 2000). In terms of the gradients of u_i, T, g_{ij}, ω_{ijk} h_i, γ_{ij} and χ, (48) can be rewritten as

$$\sigma_{ij} = -\underline{\mu \frac{\partial u_i}{\partial x_j}} - \mu \frac{\partial u_j}{\partial x_i} + \frac{2}{3}\mu \frac{\partial u_l}{\partial x_l}\delta_{ij} + \rho g_{ij}, \tag{49}$$

$$q_i = -\underline{\frac{15}{4} R\mu \frac{\partial T}{\partial x_i}} + \rho h_i, \tag{50}$$

$$\begin{aligned} m_{ijk} = &-\underline{\frac{2}{3}\mu \frac{\partial g_{ij}}{\partial x_k}} - \frac{2}{3}\mu \frac{\partial \left(\sigma_{ij}^G/\rho\right)}{\partial x_k} - \frac{2}{3}\mu \left(\frac{\partial(\sigma_{ik}/\rho)}{\partial x_j} + \frac{\partial(\sigma_{jk}/\rho)}{\partial x_i} \right) \\ &+ \frac{4}{15}\mu \left(\frac{\partial(\sigma_{ir}/\rho)}{\partial x_r}\delta_{jk} + \frac{\partial(\sigma_{jr}/\rho)}{\partial x_r}\delta_{ik} + \frac{\partial(\sigma_{kr}/\rho)}{\partial x_r}\delta_{ij} \right) + \rho\omega_{ijk}, \end{aligned} \tag{51}$$

$$R_{ij} = -\underline{\frac{12}{5}\mu \frac{\partial h_i}{\partial x_j}} - \frac{12}{5}\mu \frac{\partial \left(q_i^G/\rho\right)}{\partial x_j} - \frac{12}{5}\mu \frac{\partial(q_j/\rho)}{\partial x_i} + \frac{8}{5}\mu \frac{\partial(q_l/\rho)}{\partial x_l}\delta_{ij} + \rho\gamma_{ij}, \tag{52}$$

$$\begin{aligned} \phi_{ijkl} = &-\underline{\frac{\mu}{C_1}\frac{\partial \omega_{ijk}}{\partial x_l}} - \frac{\mu}{C_1}\frac{\partial \left(m_{ijk}^G/\rho\right)}{\partial x_l} - \frac{\mu}{C_1}\left(\frac{\partial(m_{ijl}/\rho)}{\partial x_k} + \frac{\partial(m_{jkl}/\rho)}{\partial x_i} + \frac{\partial(m_{ikl}/\rho)}{\partial x_j} \right) \\ &+ \frac{2\mu}{7C_1}\left(\frac{\partial(m_{klr}/\rho)}{\partial x_r}\delta_{ij} + \frac{\partial(m_{jlr}/\rho)}{\partial x_r}\delta_{ik} + \frac{\partial(m_{ilr}/\rho)}{\partial x_r}\delta_{jk} \right) \\ &+ \frac{2\mu}{7C_1}\left(\frac{\partial(m_{jkr}/\rho)}{\partial x_r}\delta_{il} + \frac{\partial(m_{ikr}/\rho)}{\partial x_r}\delta_{jl} + \frac{\partial(m_{ijr}/\rho)}{\partial x_r}\delta_{kl} \right) + \phi_{ijkl}^R, \end{aligned} \tag{53}$$

$$\begin{aligned} \psi_{ijk} = &-\underline{\frac{9\mu}{7Y_1}\frac{\partial \gamma_{ij}}{\partial x_k}} - \frac{9\mu}{7Y_1}\frac{\partial \left(R_{ij}^G/\rho\right)}{\partial x_k} - \frac{9\mu}{7Y_1}\left(\frac{\partial(R_{ik}/\rho)}{\partial x_j} + \frac{\partial(R_{jk}/\rho)}{\partial x_i} \right) \\ &+ \frac{18\mu}{35Y_1}\left(\frac{\partial(R_{ir}/\rho)}{\partial x_r}\delta_{jk} + \frac{\partial(R_{jr}/\rho)}{\partial x_r}\delta_{ik} + \frac{\partial(R_{kr}/\rho)}{\partial x_r}\delta_{ij} \right) + \psi_{ijk}^R \end{aligned} \tag{54}$$

and

$$\Omega_i = -\underline{\frac{7\mu}{3}\frac{\partial \chi}{\partial x_i}} - \frac{7\mu}{3}\frac{\partial(\Delta^G/\rho)}{\partial x_i} + \Omega_i^R. \tag{55}$$

Inserting (49)–(55) into (3), (4) and (43)–(47), the governing equations for the new variables are obtained after mathematical manipulation:

$$\frac{\partial \rho u_i}{\partial t} + \frac{\partial \rho u_l u_i}{\partial x_l} - \frac{\partial}{\partial x_l}\left(\mu \frac{\partial u_i}{\partial x_l}\right) = -\frac{\partial p}{\partial x_i} + \frac{\partial}{\partial x_l}\left(\mu \frac{\partial u_l}{\partial x_i}\right) - \frac{2}{3}\frac{\partial}{\partial x_i}\left(\mu \frac{\partial u_l}{\partial x_l}\right) + \rho a_i - \underline{\frac{\partial \rho g_{il}}{\partial x_l}}, \tag{56}$$

$$\frac{\partial \rho T}{\partial t} + \frac{\partial \rho u_l T}{\partial x_l} - \frac{5}{2}\frac{\partial}{\partial x_l}\left(\mu \frac{\partial T}{\partial x_l}\right) = -\frac{2}{3R}\left(p\frac{\partial u_i}{\partial x_i} + \sigma_{ij}\frac{\partial u_j}{\partial x_i}\right) - \underline{\frac{2}{3R}\frac{\partial \rho h_i}{\partial x_i}}, \tag{57}$$

$$\frac{\partial \rho g_{ij}}{\partial t}+\frac{\partial \rho u_l g_{ij}}{\partial x_l}-\frac{2}{3}\frac{\partial}{\partial x_l}\left(\mu\frac{\partial g_{ij}}{\partial x_l}\right)=-\frac{p}{\mu}\rho g_{ij}+\Sigma_{ij}-\frac{\partial \rho\omega_{ijk}}{\partial x_k}+\frac{2}{3}\frac{\partial}{\partial x_k}\left(\mu\frac{\partial(\sigma_{ik}/\rho)}{\partial x_j}\right)+\frac{2}{3}\frac{\partial}{\partial x_k}\left(\mu\frac{\partial(\sigma_{jk}/\rho)}{\partial x_i}\right)-\frac{4}{15}\frac{\partial}{\partial x_j}\left(\mu\frac{\partial(\sigma_{ir}/\rho)}{\partial x_r}\right)-\frac{4}{15}\frac{\partial}{\partial x_i}\left(\mu\frac{\partial(\sigma_{jr}/\rho)}{\partial x_r}\right)-\frac{4}{15}\frac{\partial}{\partial x_k}\left(\mu\frac{\partial(\sigma_{kr}/\rho)}{\partial x_r}\right)\times\delta_{ij}-\left\{\frac{\partial\sigma_{ij}^G}{\partial t}+\frac{\partial u_k\sigma_{ij}^G}{\partial x_k}-\frac{2}{3}\frac{\partial}{\partial x_k}\left[\mu\frac{\partial\left(\sigma_{ij}^G/\rho\right)}{\partial x_k}\right]\right\}, \tag{58}$$

$$\frac{\partial \rho h_i}{\partial t}+\frac{\partial \rho u_j h_i}{\partial x_j}-\frac{6}{5}\frac{\partial}{\partial x_j}\left(\mu\frac{\partial h_i}{\partial x_j}\right)=-\frac{2}{3}\frac{p}{\mu}\rho h_i-\frac{1}{2}\frac{\partial\rho\gamma_{ij}}{\partial x_j}+Q_i+\frac{6}{5}\frac{\partial}{\partial x_j}\left(\mu\frac{\partial(q_j/\rho)}{\partial x_i}\right)-\frac{4}{5}\frac{\partial}{\partial x_i}\left(\mu\frac{\partial(q_l/\rho)}{\partial x_l}\right)-\left\{\frac{\partial q_i^G}{\partial t}+\frac{\partial u_j q_i^G}{\partial x_j}-\frac{6}{5}\frac{\partial}{\partial x_j}\times\left(\mu\frac{\partial\left(q_i^G/\rho\right)}{\partial x_j}\right)\right\}, \tag{59}$$

$$\begin{aligned}&\frac{\partial \rho\omega_{ijk}}{\partial t}+\frac{\partial \rho u_l\omega_{ijk}}{\partial x_l}-\frac{\partial}{\partial x_l}\left(\frac{\mu}{C_1}\frac{\partial\omega_{ijk}}{\partial x_l}\right)\\&=-\frac{3}{2}\frac{p}{\mu}\rho\omega_{ijk}-\frac{\partial\phi_{ijkl}^R}{\partial x_l}+\mathfrak{M}_{ijk}+\frac{\partial}{\partial x_l}\left(\frac{\mu}{C_1}\frac{\partial(m_{ijl}/\rho)}{\partial x_k}\right)+\frac{\partial}{\partial x_l}\left(\frac{\mu}{C_1}\frac{\partial(m_{jkl}/\rho)}{\partial x_i}\right)\\&+\frac{\partial}{\partial x_l}\left(\frac{\mu}{C_1}\frac{\partial(m_{ikl}/\rho)}{\partial x_j}\right)-\frac{\partial}{\partial x_l}\left(\frac{2\mu}{7C_1}\frac{\partial(m_{klr}/\rho)}{\partial x_r}\right)\delta_{ij}-\frac{\partial}{\partial x_l}\left(\frac{2\mu}{7C_1}\frac{\partial(m_{jlr}/\rho)}{\partial x_r}\right)\\&\times\delta_{ik}-\frac{\partial}{\partial x_l}\left(\frac{2\mu}{7C_1}\frac{\partial(m_{ilr}/\rho)}{\partial x_r}\right)\delta_{jk}-\frac{\partial}{\partial x_i}\left(\frac{2\mu}{7C_1}\frac{\partial(m_{jkr}/\rho)}{\partial x_r}\right)-\frac{\partial}{\partial x_j}\left(\frac{2\mu}{7C_1}\frac{\partial(m_{ikr}/\rho)}{\partial x_r}\right)\\&-\frac{\partial}{\partial x_k}\left(\frac{2\mu}{7C_1}\frac{\partial(m_{ijr}/\rho)}{\partial x_r}\right)-\left\{\frac{\partial m_{ijk}^G}{\partial t}+\frac{\partial u_l m_{ijk}^G}{\partial x_l}-\frac{\partial}{\partial x_l}\left(\frac{\mu}{C_1}\frac{\partial\left(m_{ijk}^G/\rho\right)}{\partial x_l}\right)\right\},\end{aligned} \tag{60}$$

$$\begin{aligned}&\frac{\partial \rho\gamma_{ij}}{\partial t}+\frac{\partial \rho u_l\gamma_{ij}}{\partial x_l}-\frac{9}{7}\frac{\partial}{\partial x_l}\left(\frac{\mu}{Y_1}\frac{\partial\gamma_{ij}}{\partial x_l}\right)\\&=-\frac{7}{6}\frac{p}{\mu}\rho\gamma_{ij}-\frac{\partial\psi_{ijk}^R}{\partial x_k}+\mathfrak{R}_{ij}+\frac{9}{7}\frac{\partial}{\partial x_k}\left(\frac{\mu}{Y_1}\frac{\partial(R_{ik}/\rho)}{\partial x_j}\right)+\frac{9}{7}\frac{\partial}{\partial x_k}\left(\frac{\mu}{Y_1}\frac{\partial(R_{jk}/\rho)}{\partial x_i}\right)\\&-\frac{18}{35}\frac{\partial}{\partial x_j}\left(\frac{\mu}{Y_1}\frac{\partial(R_{ir}/\rho)}{\partial x_r}\right)-\frac{18}{35}\frac{\partial}{\partial x_i}\left(\frac{\mu}{Y_1}\frac{\partial(R_{jr}/\rho)}{\partial x_r}\right)-\frac{18}{35}\frac{\partial}{\partial x_k}\left(\frac{\mu}{Y_1}\frac{\partial(R_{kr}/\rho)}{\partial x_r}\right)\delta_{ij}\\&-\left\{\frac{\partial R_{ij}^G}{\partial t}+\frac{\partial u_k R_{ij}^G}{\partial x_k}-\frac{\partial}{\partial x_k}\left(\frac{9\mu}{7Y_1}\frac{\partial\left(R_{ij}^G/\rho\right)}{\partial x_k}\right)\right\}\end{aligned} \tag{61}$$

and

$$\frac{\partial \rho \chi}{\partial t} + \frac{\partial \rho u_i \chi}{\partial x_i} - \frac{7}{3}\frac{\partial}{\partial x_i}\left(\mu \frac{\partial \chi}{\partial x_i}\right) = -\frac{2}{3}\frac{p}{\mu}\rho\chi - \frac{\partial \Omega_i^R}{\partial x_i} + \aleph - \left\{\frac{\partial \Delta^G}{\partial t} + \frac{\partial u_i \Delta^G}{\partial x_i} - \frac{\partial}{\partial x_i}\left(\frac{7\mu}{3}\frac{\partial(\Delta^G/\rho)}{\partial x_i}\right)\right\}. \quad (62)$$

The primitive variables of the moment equations have been transformed from $\{\rho, u_i, T, \sigma_{ij}, q_i, m_{ijk}, R_{ij}, \Delta\}$ to $\{\rho, u_i, T, g_{ij}, h_i, \omega_{ijk}, \gamma_{ij}, \chi\}$. The resultant equations (56)–(62) now have the following general convection–diffusion form:

$$\underbrace{\frac{\partial \rho \Phi}{\partial t}}_{\text{transition}} + \underbrace{\frac{\partial \rho u_l \Phi}{\partial x_l}}_{\text{convection}} - \underbrace{\frac{\partial}{\partial x_l}\left(\frac{\mu}{\Gamma_\Phi}\frac{\partial \Phi}{\partial x_l}\right)}_{\text{diffusion}} = \underbrace{\frac{S_\Phi}{\text{source}}}, \quad (63)$$

in which $\Phi = (u_i, T, g_{ij}, h_i, \omega_{ijk}, \gamma_{ij}, \chi)$; $\Gamma_\Phi = (1, 2/5, 3/2, 5/6, C_1, 7Y_1/9, 3/7)$; and $S_\Phi = (S_{u_i}, S_T, S_{g_{ij}}, S_{h_i}, S_{\omega_{ijk}}, S_{\gamma_{ij}}, S_\chi)$ corresponds to the right-hand terms of (56)–(62). These equations form a set of second-order PDEs. The mathematical characteristics of the system is determined by the flow conditions. They are of a hyperbolic nature for high-speed flows and parabolic or elliptic when the flow velocity is low or the flow is recirculating.

5.2. *Numerical solution procedure*

The moment method results in a set of equations in a conventional convection–diffusion format, with appropriate source terms, which can be used to capture non-equilibrium phenomena. In most situations, there are no analytical solutions for this complex set of PDEs, and a numerical procedure is therefore required. Numerical methods for solving the convective and diffusion equations are well documented for both high- and low-speed flows (Ferziger & Peri 1999; Toro 1999). Equations (56) and (57) are similar to the NSF equations but with extra terms underlined on the right-hand side that account for any non-equilibrium effects, and these can be determined from the rest of the equation set. An NSF solver can be modified to solve the 26 moment equations by adding the extra source terms to the momentum and energy equations and treating the individual components of the remaining variables as scalars. In the present study, the finite-volume approach has been employed, and the diffusive and source terms are discretized by a central difference scheme. For the convective terms, a range of upwind schemes including QUICK (Leonard 1979), SMART (Gaskell & Lau 1988) and CUBISTA (Alves, Oliveira, & Pinho 2003) are described in the literature, and the CUBISTA scheme was selected for the present study. The coupling of the velocity and pressure fields is through the SIMPLE algorithm (Patankar 1980). A collocated grid arrangement is used, and the interpolation scheme of Rhie & Chow (1983) is employed to eliminate any non-physical pressure oscillations. For steady-state flow, the system of equations can be solved iteratively, and the solution procedure is summarized as follows:

(i) Solve u_i at iteration $n+1$ using the values of other variables at the previous iteration n.

(ii) Solve the pressure correction equation using the SIMPLE algorithm to update p and u_i at iteration $n+1$.

(iii) Solve T, g_{ij}, h_i, ω_{ijk}, γ_{ij}, χ at iteration $n+1$ using updated pressure and velocity fields.

(iv) Calculate values of the moments σ_{ij}, q_i, m_{ijk}, R_{ij}, Δ from (48).

(v) Update the boundary conditions according to (32), (33) and (C1)–(C8).

(vi) Return to step 1 and repeat until residuals of each governing equation reach a specified convergence criterion.

Computationally, it is more expensive to solve the R26 equations than the NSF equations, but this cost is necessary to capture non-equilibrium phenomena. However, the advanced computational and numerical techniques developed over the years for conventional computational fluid dynamics can be readily adopted so that the moment method can be applied for engineering applications in which non-equilibrium effects are important, in particular, in the low-speed, low-Reynolds-number regime in which it can be costly and difficult to get meaningful statistical data from stochastic methods.

6. Results and discussion

The R26 equations, along with the NSF equations and the regularized 13 moment equations (R13), have been used to compute both planar Couette and Poiseuille flows for argon gas. The first-order velocity-slip and temperature-jump boundary conditions for the NSF equations have been taken from Cercignani (1988). The viscosity was obtained from Sutherland's law (White 1991):

$$\mu = \mu_o \left(\frac{T}{T_o}\right)^{1.5} \frac{T_o + S}{T + S}, \tag{64}$$

where the reference viscosity and temperature are $\mu_o = 21.25 \times 10^{-6}$ Pa s and $T_o = 273$ K, respectively. The specific gas constant and Sutherland's constant for argon are $R = 208$ J (kg K)$^{-1}$ and $S = 144$ K. The molecular mean free path is given by (Cercignani 1988)

$$\lambda = \frac{\mu}{p}\sqrt{\frac{\pi RT}{2}}. \tag{65}$$

In the present study, the coordinates are chosen such that the walls are parallel to the x-direction and y is the direction perpendicular to the plates. The distance between the two parallel plates is H, and the two plates have been set at $y = \pm H/2$. The Knudsen number is given by $Kn = \lambda/H$. The accommodation coefficient α is assigned a value of unity; i.e. fully diffuse reflection has been assumed for both walls. In the case of planar Couette flow, the upper and lower plates move with a constant velocity $u_w = \pm 50$ m s^{-1}, in opposite directions, and the external acceleration $a_x = a_y = 0$. The flow is solved with a one-dimensional grid using 200 equispaced grid points across the domain. Data obtained from DSMC calculations (Bird 1994) are used to assess the capability and limitations of the hydrodynamic models, particularly in the transition regime. In the case of pressure-driven Poiseuille flow, both plates are stationary and a pressure gradient is applied in the x-direction. Using the centreline as a symmetry, only half of the flow is solved. The flow is solved using a two-dimensional grid with 10×100 uniformly spaced grid points. For this case, the hydrodynamic results are compared with the data obtained by Ohwada *et al.* (1989) using the Boltzmann equation. In all cases, the wall temperature is fixed at $T_w = 273$ K.

6.1. *Planar Couette flow in the transition regime*

Figure 1 shows the computed velocity profiles for planar Couette flow. Results are presented for Knudsen numbers $Kn = 0.1, 0.2, 0.5, 0.75$ and 1.0. At the upper limit of the slip regime, $Kn = 0.1$, and early transition regime, $Kn = 0.25$, the velocity profile predicted by the NSF and R13 equations is linear, as indicated in figure 1(a,b). In

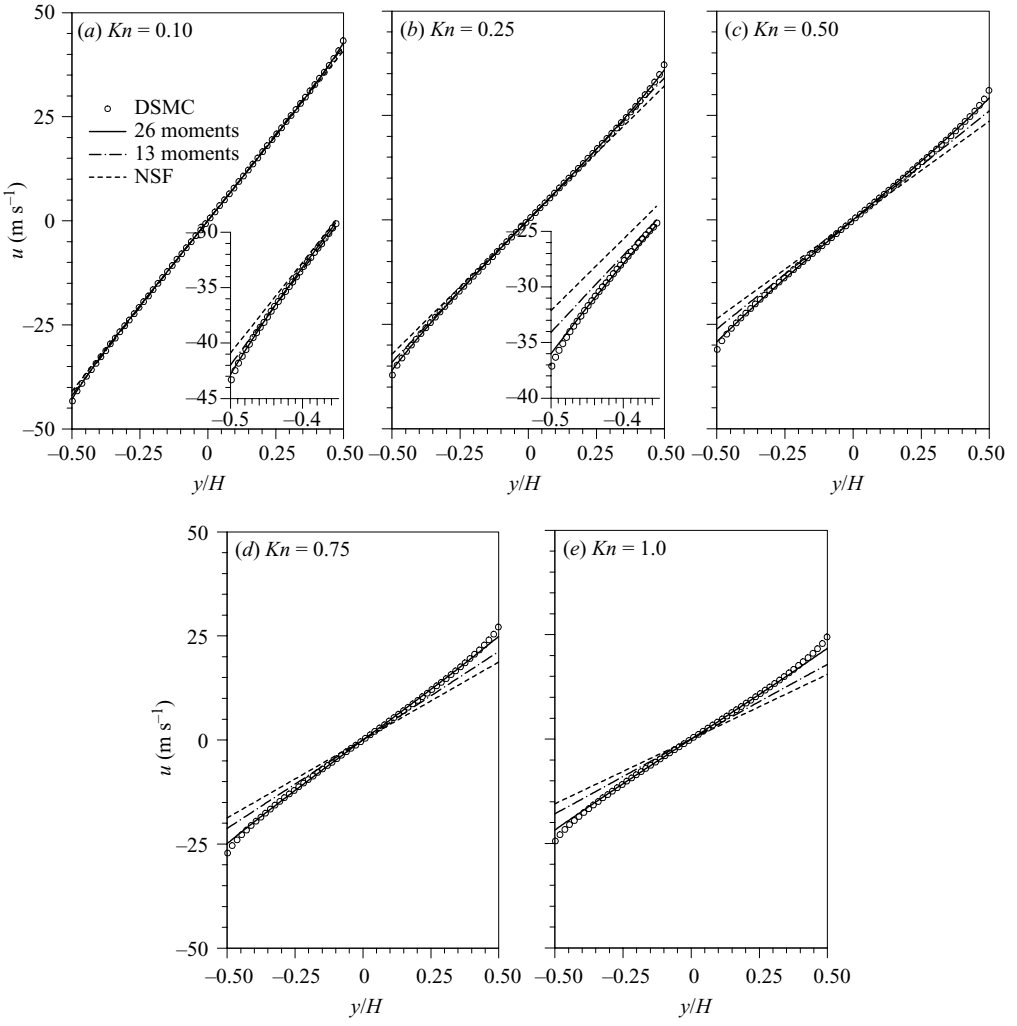

FIGURE 1. Predicted velocity profiles at a range of Knudsen numbers for Couette flow with initial conditions, $T_w = 273$ K and $u_w = \pm 50$ m s^{-1}: ○, DSMC; ——, R26; ——·——·, R13; - - - - -, NSF.

the core part of the flow (i.e. outside of the Knudsen layer), all three models are in agreement with the DSMC data. However, in the region close to the wall, the DSMC results indicate a Knudsen-layer velocity profile, as shown in the enlarged part in figure 1(a, b). Neither the NSF nor the R13 equations follow this behaviour, whilst the R26 equations are in excellent agreement with the DSMC data. At $Kn = 0.5$ and above, well into the transition regime, the DSMC data clearly show the expected Knudsen-layer velocity profile with substantial velocity slip at the surface due to strong rarefaction effects. Both the R13 and NSF equations fail to capture this aspect of the velocity profile, and both methods overpredict the amount of velocity slip, although the value predicted by the R13 equations is in better agreement with the DSMC data than the NSF results, as illustrated in figure 1(c). In contrast, the results from the R26 equations are in very good agreement with the DSMC data, and the new model not only predicts the correct velocity slip but also, and more importantly,

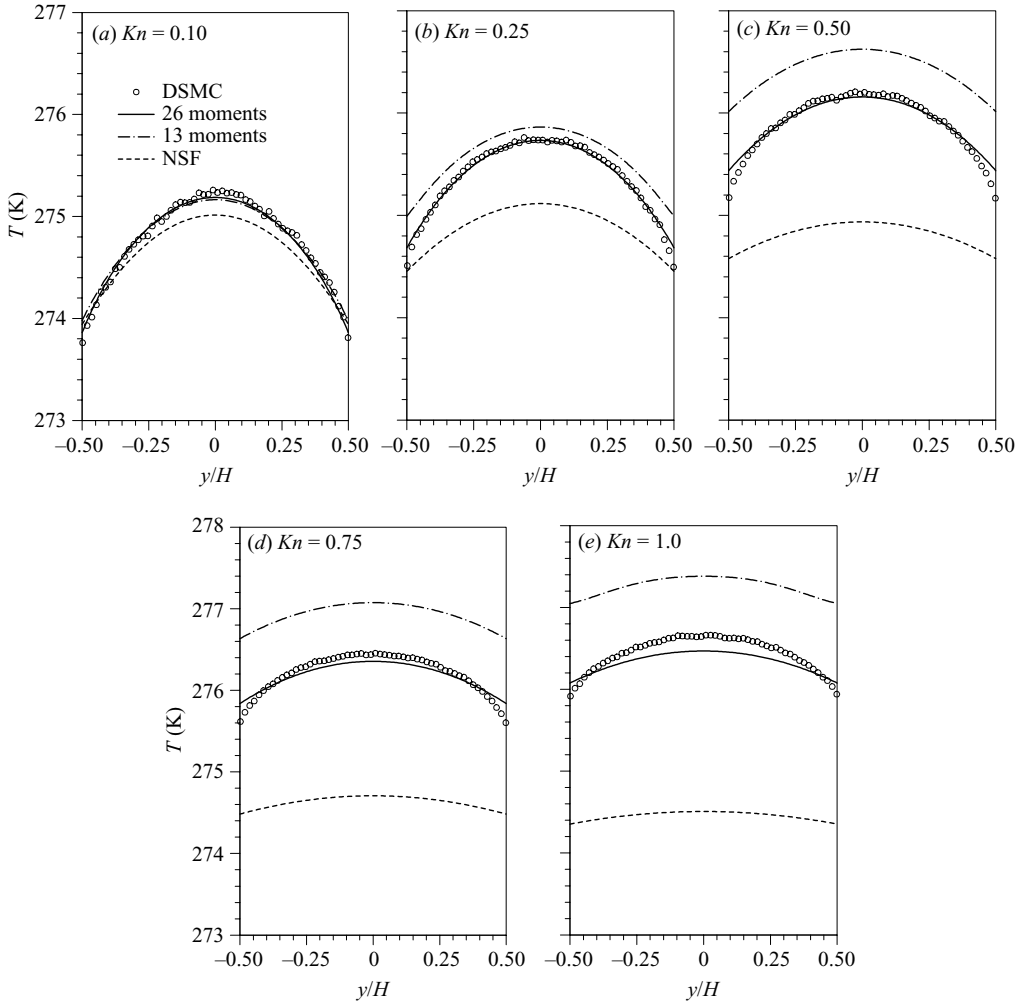

FIGURE 2. Predicted temperature profiles at a range of Knudsen numbers for Couette flow with initial conditions, $T_w = 273\,\mathrm{K}$ and $u_w = \pm 50\,\mathrm{m\,s^{-1}}$: ○, DSMC; ——, R26; —·—·, R13; - - - - -, NSF.

captures the power-law behaviour of the velocity profile in the Knudsen layer (Lilley & Sader 2007, 2008), even up to $Kn = 1.0$, as indicated in figure 1(*d*, *e*). The improved predictive capability of the R26 equations arises from their fifth-order accuracy in Kn, whilst the R13 equations are only third order. As highlighted by Struchtrup (2008), Knudsen layers in the moment method appear as superpositions of exponentials of different width. The R13 system is the lowest moment system to describe both the GTM and the NGTM in the transition regime and therefore produces only one such contribution (Struchtrup & Torrilhon 2008). The R26 equations can model the Knudsen-layer velocity profile more accurately due to the extra boundary-layer contribution from m_{ijk}.

Figure 2 shows the temperature profiles at the five different Knudsen numbers. The NSF equations consistently underpredict the temperature field in the transition regime and particularly at larger values of Kn. The R13 equations are only in good agreement with the DSMC data at $Kn = 0.1$ and overpredict the temperature field

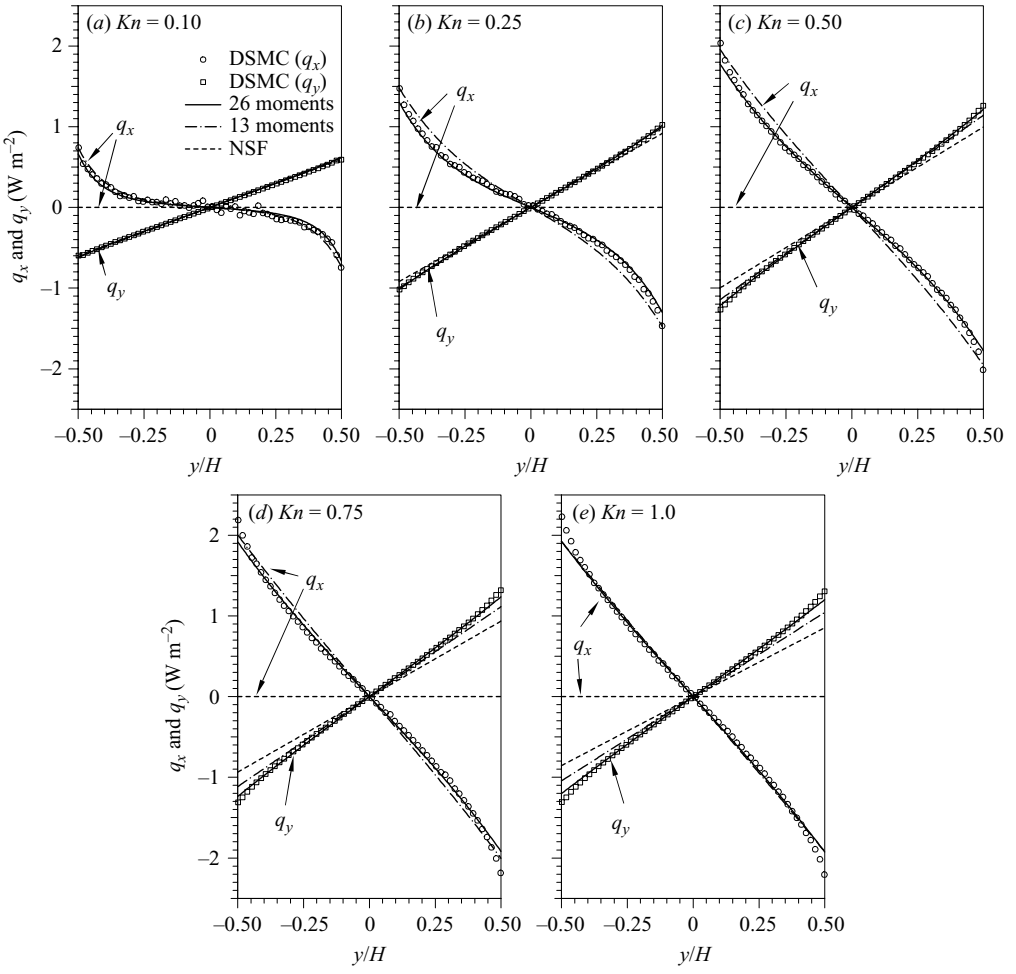

FIGURE 3. Profiles of tangential and normal heat fluxes q_x and q_y for Couette flow with initial conditions, $T_w = 273$ K and $u_w = \pm 50\,\mathrm{m\,s^{-1}}$: ○, □, DSMC; ——, R26; —·—·—, R13; - - - - -, NSF.

significantly for Kn above 0.25, as shown in figure 2(*b–e*), whereas the temperature fields predicted by the R26 equations are close to the DSMC data up to $Kn = 0.75$. At $Kn = 1.0$, the R26 model is in good agreement for the value of the temperature jump but slightly underpredicts the temperature in the central region of the flow. The improved prediction of temperature by the R26 equations is clearly very significant.

The profiles of the second-moment variables are presented in figures 3 and 4. An interesting non-equilibrium phenomenon that occurs in planar Couette flow is the appearance of a heat flux without the presence of a temperature gradient, i.e. non-gradient transport, and this is illustrated in figure 3, which shows both the normal and tangential heat fluxes. As indicated by the DSMC data, a significant amount of tangential heat flux q_x is generated at the upper limit of the slip regime. This is shown in figure 3(*a*) in which both the R13 and R26 models are in good agreement with the DSMC data. However, the NSF equations are not able to predict this aspect of the flow. In particular, the values of q_x obtained from the R13 and R26 equations follow the DSMC data right up to the near-wall region for Knudsen numbers up to 1.0, as shown in figure 3(*b–e*). However, the normal heat flux q_y is captured by all

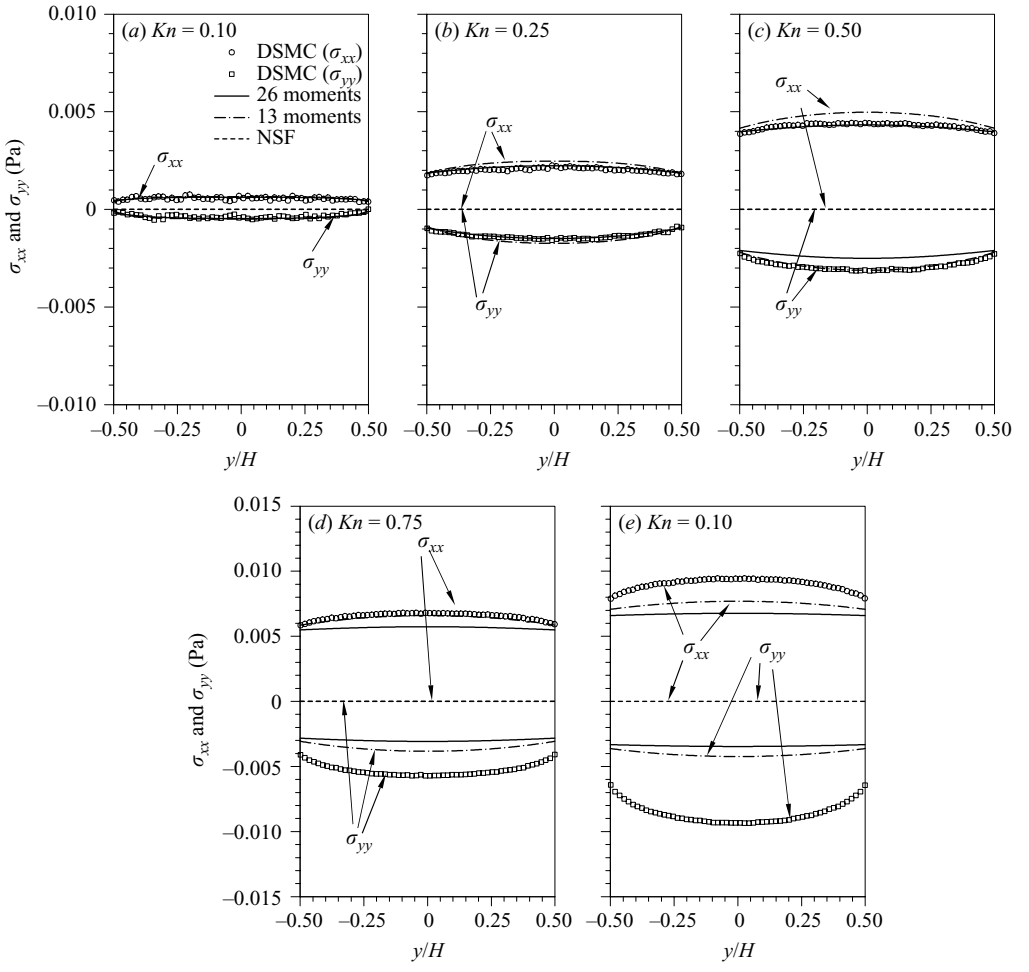

FIGURE 4. Computed profiles of normal stresses σ_{xx} and σ_{yy} for Couette flow with initial conditions, $T_w = 273\,\mathrm{K}$ and $u_w = \pm 50\,\mathrm{m\,s^{-1}}$: ○, □, DSMC; ——, R26; ——·——·, R13; - - - - -, NSF.

of the continuum-based schemes and particularly well by the R13 and R26 models when $Kn \leqslant 0.25$. Only the R26 equations follow the DSMC data at larger Knudsen numbers.

Another important non-equilibrium phenomenon that appears in planar Couette flow is the non-zero values of the normal components of stress σ_{xx} and σ_{yy}. As indicated in figure 4, the NSF equations produce a value of zero for both normal stresses at all values of Kn, whilst the DSMC results demonstrate that both σ_{xx} and σ_{yy} are no longer zero when the flow is in the transition regime. This effect is due to the impact of the NGTM. Both higher-order models are able to capture this departure from equilibrium reasonably well up to $Kn = 0.5$, as shown in figure 4(a–c). However, as the Knudsen number increases, both the R13 and R26 equations start to deviate from the values of σ_{xx} and σ_{yy} predicted by DSMC, as shown in figure 4(d, e), but are still able to follow the basic trend.

One particular feature of planar Couette flow is having a constant shear stress throughout the domain. Shown in figure 5 is the shear stress σ_{xy} predicted by the

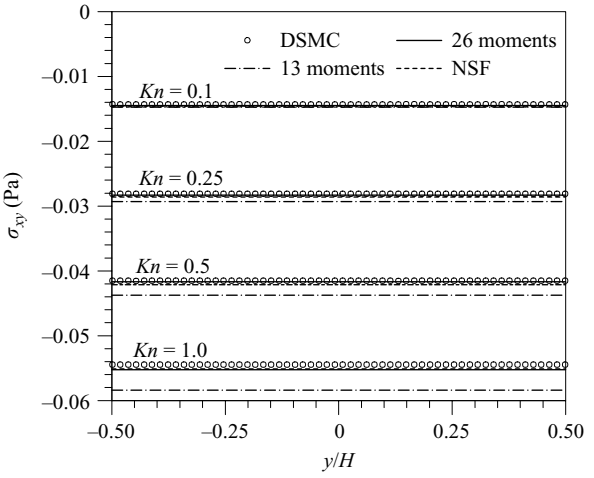

FIGURE 5. Computed profiles of shear stress σ_{xy} for Couette flow with initial conditions, $T_w = 273$ K and $u_w = \pm 50$ m s^{-1}: ○, DSMC; ——, R26; —·—·, R13; - - - - -, NSF.

moment equations in comparison with the DSMC results for four different Knudsen numbers. All three models predict a value of σ_{xy} close to the DSMC data apart from the R13 equations which overpredict the value of σ_{xy} by about 5 % at $Kn = 0.5$ and 7 % at $Kn = 1.0$. The predicted values of σ_{xy} from the NSF equations appear to be in good agreement with the DSMC data, but it must be remembered that the values of σ_{xy} predicted by the NSF equations are evaluated from incorrect velocity profiles, as illustrated in figure 1. The R26 equations clearly provide a significant improvement in the prediction of the shear stress when compared to the R13 equations, particularly in the transition regime, because of the extra contribution to the Knudsen-layer velocity profile from the boundary layer generated by m_{xyy}, which will be discussed next.

The profiles of the higher moments m_{ijk} are presented in figure 6. When $Kn \leqslant 0.5$, both the R13 and R26 models predict m_{xxy} quite well in comparison to the DSMC data, with the R26 model slightly better than the R13 equations, as shown in figure 6(a–c). At $Kn = 0.75$ and 1.0, the profiles of m_{xxy} predicted by the R26 equations still capture the basic trend but are clearly not as close to the DSMC data as the results at lower values of Knudsen number. However, the prediction of m_{xyy} is improved significantly by the R26 equations, as indicated in figure 6. The predictions for m_{xyy} produced by the R13 equations are close to zero in the transition regime and are unable to follow the trend of the DSMC data, which leads to their failure to predict the velocity profile correctly in the Knudsen layer. However, the R26 equations follow the DSMC data closely, but the agreement starts to deteriorate when $Kn \geqslant 0.5$, as shown in figure 6(c–e). In addition to a constant shear stress σ_{xy} in steady-state planar Couette flow, the value of $p_2 = p + \sigma_{yy}$ is also constant. From (7) the velocity is readily expressed as

$$u = -\frac{p}{p_2}\frac{\sigma_{xy}}{\mu}y - \frac{1}{p_2}\left(m_{xyy} + \frac{2}{5}q_x\right) + \text{boundary conditions.} \tag{66}$$

It is obvious that the velocity consists of the contributions from σ_{xy}, q_x and m_{xyy}. As in the R13 equations, there is no mechanism for m_{xyy} to produce a boundary layer; so the Knudsen-layer contribution is solely from q_x, whilst the Knudsen-layer contribution in the R26 system is from both q_x and m_{xyy}. Furthermore, comparing

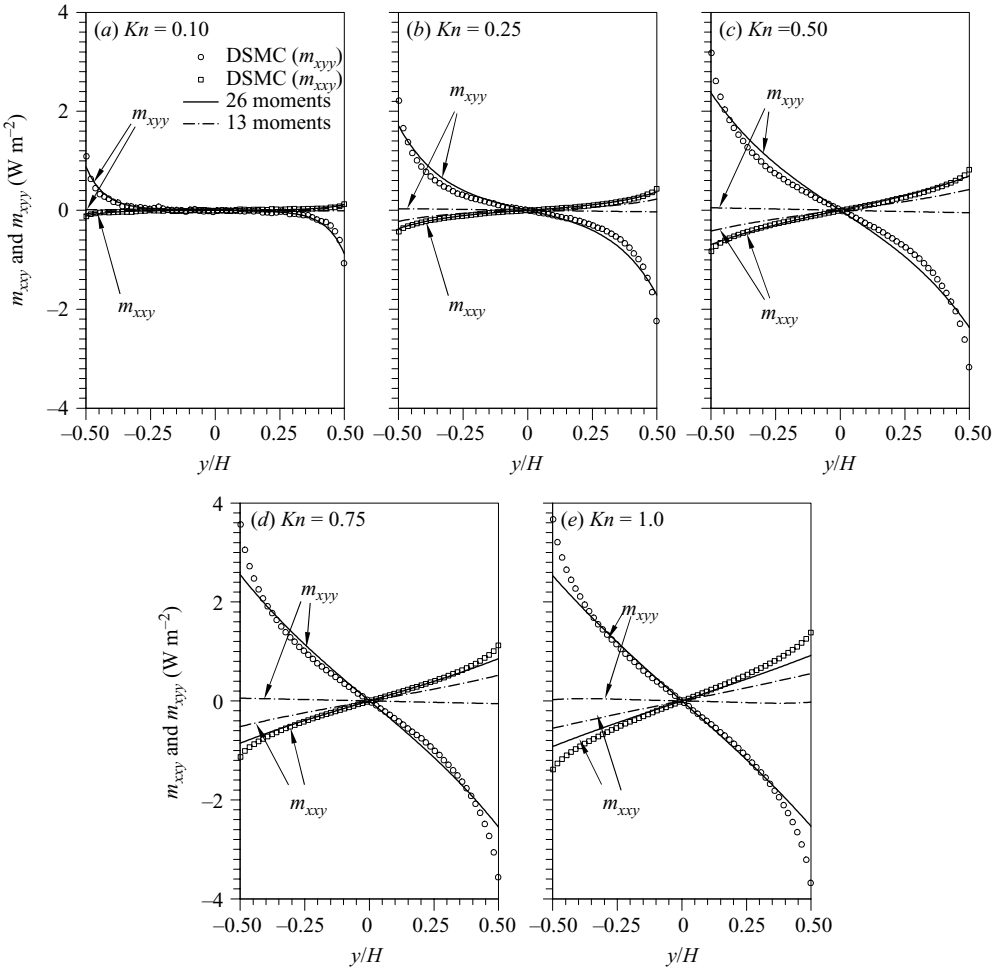

FIGURE 6. Profiles m_{xxy} and m_{xyy} for Couette flow with $T_w = 273$ K and $u_w = \pm 50$ m s^{-1}: ○, □, DSMC; ——, R26; —·—·, R13.

the magnitude of q_x and m_{xyy} in figures 3 and 6 indicates that the impact of m_{xyy} on the Knudsen-layer velocity is greater than that of q_x. An accurate prediction of m_{xyy} is clearly essential to correctly describe the Knudsen-layer velocity profile.

To ensure that no unphysical solutions are obtained in the above results, the eigenvalues of the validity matrix (35) and the production of the entropy are calculated for the R26 moment equations. The eigenvalues of the matrix (35), λ_1 (positive square root) and λ_2 (negative square root), for one-dimensional planar Couette flow are

$$\lambda_{1,2} = \frac{1}{2}\left[(V_{xx} + V_{yy}) \pm \sqrt{(V_{xx} - V_{yy})^2 + 4V_{xy}^2}\right], \tag{67}$$

in which $V_{xx} = 1 + (\sigma_{xx}/p) - (2q_x^2/p(3pRT + \Delta/2))$, $V_{yy} = 1 + (\sigma_{yy}/p) - (2q_y^2/p(3pRT + \Delta/2))$ and $V_{xy} = (\sigma_{xy}/p) - (2q_x q_y/p(3pRT + \Delta/2))$.

Both eigenvalues are larger than zero for the above cases as shown in figure 7(*a*), which means the stresses and heat fluxes predicted by the R26 model are realizable. As Kn increases, the values of both λ_1 and λ_2 depart from unity, with λ_2 decreasing whilst λ_1 increases. The deviation of the eigenvalues from unity is an indication of the flow

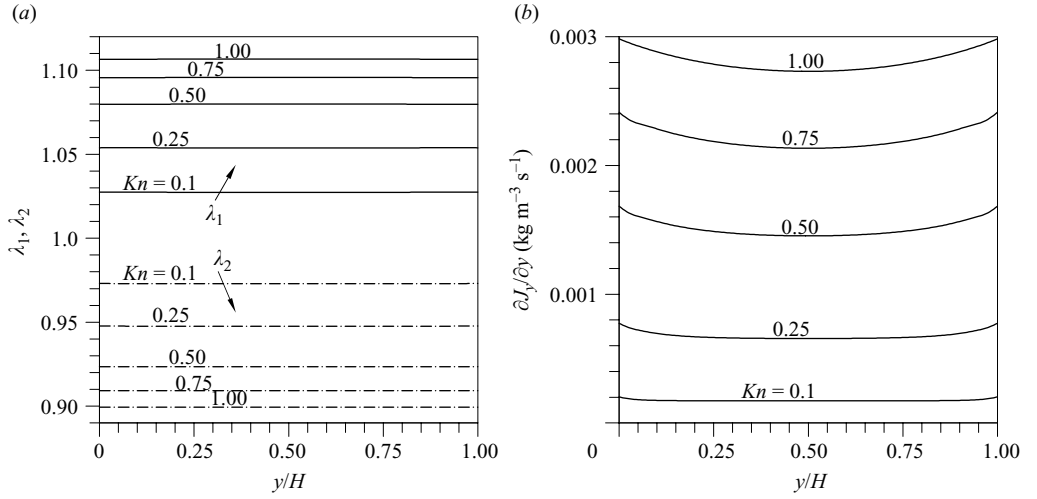

FIGURE 7. The computed values of (*a*) eigenvalues of matrix (35) and (*b*) entropy production for planar Couette flow with $T_w = 273$ K and $u_w = \pm 50$ m s^{-1} from the R26 model results.

departing from the equilibrium state (Levermore *et al.* 1998). The entropy production for the one-dimensional planar Couette flow $\partial J_y/\partial y$ is positive, as indicated in figure 7(*b*), and the Boltzmann inequality (42) is therefore satisfied.

6.2. *Poiseuille flow in the transition regime: pressure driven*

In our analysis of the flow between two parallel plates driven by a pressure gradient, with $a_x = a_y = 0$, only half of the channel is computed, and a symmetry boundary condition is employed at $y = 0$. The second-order velocity-slip boundary condition from Hadjiconstantinou (2005) is used in the Poiseuille flow study for comparison. For consistency with the conditions used by Ohwada *et al.* (1989), the applied pressure gradient is small enough that the computed temperature field is uniform. The velocity u is non-dimensionalized by $u_o = \zeta\sqrt{2RT}$ (Xu & Li 2004), where ζ is related to the pressure gradient in the channel by $p = p_o(1 - \zeta x/H)$. The mass flow rate Q has been non-dimensionalized by $Q_o = \rho_o u_o H$, where ρ_o and p_o are the inlet density and pressure, respectively.

The velocity profile at a range of Knudsen numbers is presented in figure 8. At $Kn = 0.113$, which is just beyond the slip-flow regime, the three hydrodynamic models predict similar values of velocity and are all close to the solution obtained from the Boltzmann equation. The NSF equations with both first- and second-order boundary conditions slightly overpredict the velocity slip and underpredict the maximum velocity at the centre of the channel, as shown in figure 8(*a*). The R13 equations predict a velocity slip close to that of the NSF equations with a first-order boundary condition and a maximum velocity close to that by the NSF equations with the second-order boundary condition. The R26 equations are close to that predicted by the Boltzmann equation, but slightly overpredict the maximum velocity. However, as the value of Kn increases and the flow enters the transition regime, the NSF equations fail to predict the value of the velocity at the wall as well as in the bulk flow region, as illustrated in figure 8(*b–f*). They either underpredict the maximum velocity with the first-order boundary condition or overpredict the velocity slip with the second-order boundary condition. The velocity profile obtained from the R13 equations lies close to the NSF equations using the second-order boundary condition.

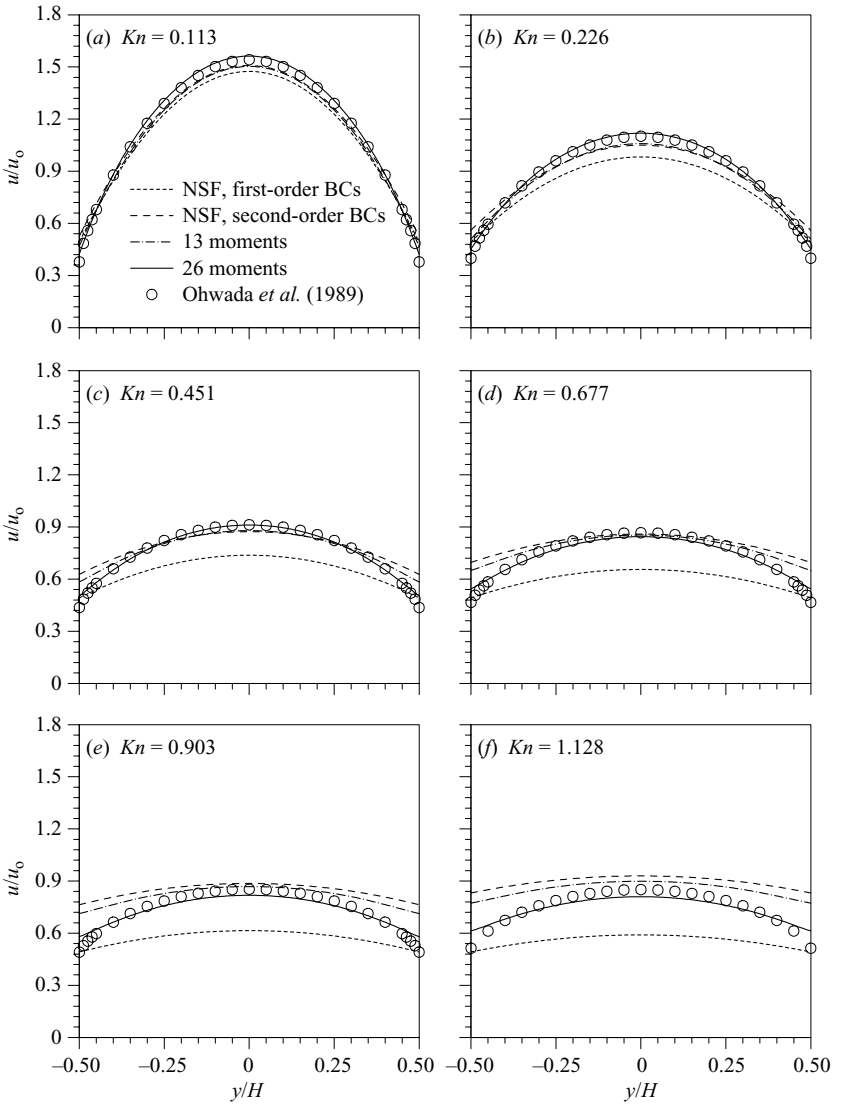

FIGURE 8. Comparison of predicted velocity profiles of pressure-driven Poiseuille flow at different values of Knudsen number: ○, Boltzmann equation solution (Ohwada *et al.* 1989); ——, R26; —·—·—, R13; - - - - -, NSF (first-order boundary conditions or BCs); – – – –, NSF (second-order BCs).

In contrast, the velocity fields predicted by the R26 equations compare very well to the solution obtained from the Boltzmann equation for both $Kn = 0.226$ and 0.451, as shown in figure 8(b, c). The velocity slip predicted by the R26 equations is in reasonable agreement with the value predicted by the Boltzmann equation, but discrepancies in the bulk flow begin to show at $Kn = 0.903$ (figure 8e) and differ at $Kn = 1.128$, as shown in figure 8(f).

In the present study, the pressure gradient is very small, and (3) can be reduced to

$$\frac{\partial \sigma_{xy}}{\partial y} = -\frac{\partial p}{\partial x} \quad \text{and} \quad \frac{\partial \sigma_{yy}}{\partial y} = -\frac{\partial p}{\partial y}; \tag{68}$$

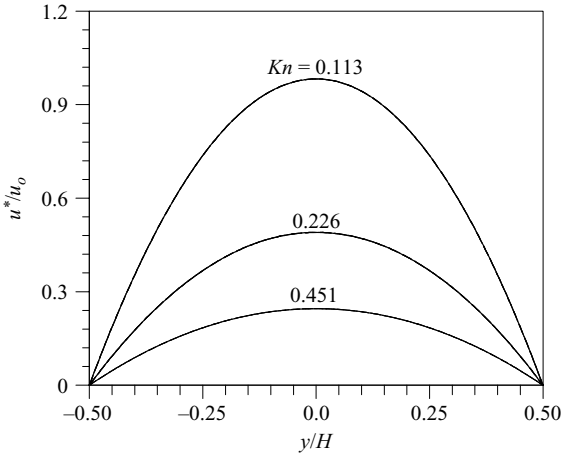

FIGURE 9. Predicted bulk contribution to the velocity profile by three hydrodynamic models at different values of Knudsen number for pressure-driven Poiseuille flow: ——, R26; —·—·, R13; - - - -, NSF (first-order BCs); – – – –, NSF (second-order BCs).

hence,

$$\sigma_{xy} = -\frac{\partial p}{\partial x} y \quad \text{and} \quad p + \sigma_{yy} = p_2 = \text{constant}. \tag{69}$$

The stress equation (7) can also be reduced to

$$\frac{\partial m_{xyy}}{\partial y} = -\frac{p}{\mu}\sigma_{xy} - p_2 \frac{\partial u}{\partial y} - \frac{2}{5}\frac{\partial q_x}{\partial y}. \tag{70}$$

For convenience, it is assumed that p/μ does not vary across the channel section and that $p/p_2 \approx 1$, so that the velocity can be approximated from (70) by

$$u \approx u_{slip} - \underbrace{\frac{1}{p_2}\left(m_{xyy} + \frac{2}{5}q_x - m^w_{xyy} - \frac{2}{5}q^w_x\right)}_{u_{Klayer}} - \underbrace{\frac{H^2}{2\mu}\frac{\partial p}{\partial x}\left(\frac{1}{4} - \frac{y^2}{H^2}\right)}_{u^*}. \tag{71}$$

Here, u_{slip} is the velocity slip at the wall and m^w_{xyy} and q^w_x are the values of m_{xyy} and q_x at the wall, respectively, which can be determined from the boundary conditions. The terms on the right-hand side of (71) can be categorized into three groups u_{slip}, u_{Klayer} and u^* to account for contributions to the velocity profile from velocity slip, the Knudsen layer and the bulk flow, respectively. The bulk contribution can be expressed in a normalized form as

$$\frac{u^*}{u_o} = -\frac{H^2}{2\mu}\frac{\partial p}{\partial x}\frac{1}{u_o}\left[\frac{1}{4} - \left(\frac{y}{H}\right)^2\right] = \frac{1}{4}\frac{\sqrt{\pi}}{Kn}\left[\frac{1}{4} - \left(\frac{y}{H}\right)^2\right]. \tag{72}$$

The profiles of u^*/u_o for $Kn = 0.113$, 0.451 and 0.677 are plotted in figure 9. As expected, the three hydrodynamic models produce identical values for each corresponding Knudsen number. As the value of Kn increases, the maximum value of u^*/u_o decreases, inversely proportional to Kn. This is not surprising, since u^*/u_o essentially describes the equilibrium component of the flow and is naturally embedded in all three hydrodynamic models. The stronger the rarefaction effects become, the less u^*/u_o will contribute to the total velocity profile.

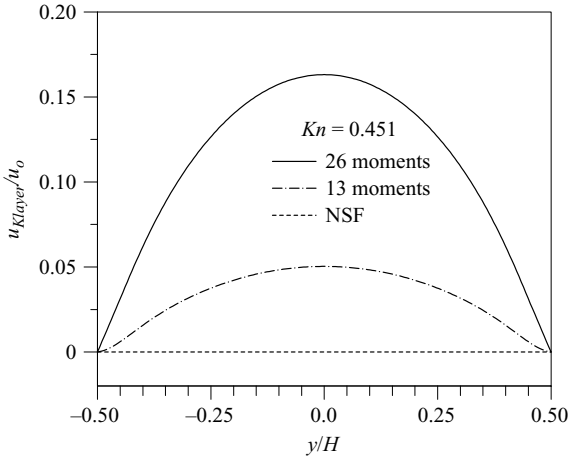

FIGURE 10. Predicted Knudsen-layer contribution to the velocity profile by three hydrodynamic models at $Kn = 0.451$: ——, R26; ——·——, R13; - - - - -, NSF (first- and second-order BCs).

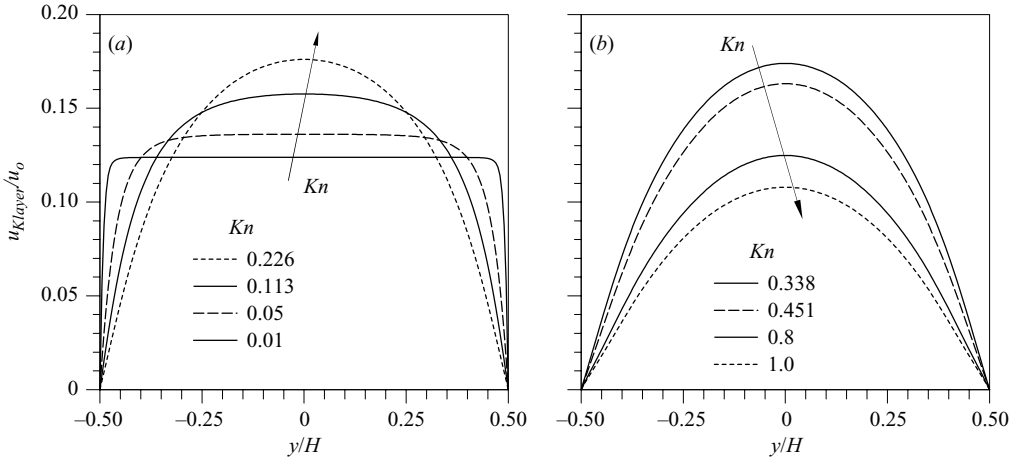

FIGURE 11. Predicted Knudsen-layer contribution to the velocity profile by R26 equations at different values of Kn: (*a*) $Kn < 0.25$; (*b*) $Kn > 0.25$.

The superposition of the Knudsen-layer contributions from q_x and m_{xyy} is clearly expressed by (71). The profiles of u_{Klayer}/u_o for $Kn = 0.451$ are plotted in figure 10. For the NSF model, $u_{Klayer} = 0$ for all values of Kn, since there is no mechanism in the NSF equations to produce a Knudsen layer. The contribution to the Knudsen layer by the R13 model is much less than that by the R26 model due to the fact that there is no mechanism in the R13 model to produce a boundary layer for m_{xyy}. In contrast, the R26 equations produce a smooth rise for u_{Klayer}/u_o which results in the smooth velocity profile shown in figure 8(*c*), in good agreement with the data from the Boltzmann equation. The effect of the Knudsen number on u_{Klayer}/u_o is illustrated in figure 11(*a*, *b*) for $Kn < 0.25$ and $Kn > 0.25$, respectively. The Knudsen layer at $Kn = 0.01$ is a thin region close to the wall, as indicated by the rising of u_{Klayer}/u_o from zero to a constant positive value within a normalized thickness around 0.05. As the value of Kn steadily increases up to 0.226, the Knudsen layer becomes thicker and

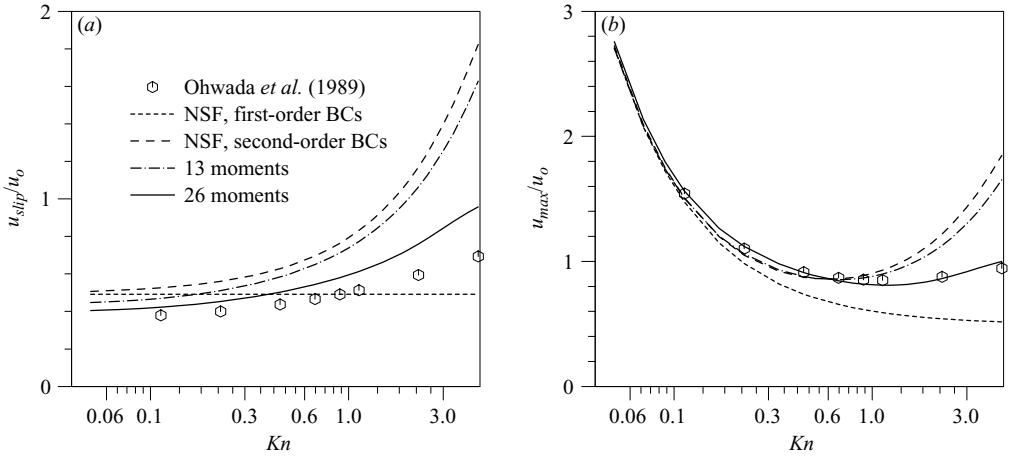

FIGURE 12. Predicted slip and maximum velocities at different values of Kn for pressure-driven Poiseuille flow: symbol, Boltzmann equation solution (Ohwada *et al.* 1989); ——, R26; —·—·, R13; - - - - -, NSF (first-order BCs); – – – – –, NSF (second-order BCs).

the maximum value of u_{Klayer}/u_o increases, as shown in figure 11(a). For $Kn \geqslant 0.338$, the influence of the Knudsen layer spreads throughout the channel, as indicated in figure 11(b), and the maximum value of u_{Klayer}/u_o begins to decrease as Kn increases beyond 0.338. The precise extent of the Knudsen layer is not known, but a reasonable estimation is 1.5λ (Hadjiconstantinou 2006), which is in good agreement with the R26 prediction. Due to the contribution from the Knudsen layer, the velocity profiles presented in figure 10 are no longer parabolic.

The values for u_{slip}/u_o predicted by the NSF, R13 and R26 equations are plotted against Kn in figure 12(a) and are compared to data obtained from the Boltzmann equation (Ohwada *et al.* 1989), which indicates that the slip velocity rises slightly as the value of Kn increases. The values of u_{slip}/u_o predicted by the NSF equations with the first-order boundary condition are constant and predict a higher velocity slip when $Kn < 1$ but underpredict the velocity slip when $Kn > 1$. Both the NSF model with the second-order boundary condition and the R13 model overpredict the velocity slip significantly, particularly at large Knudsen numbers. In comparison, the results obtained from the R26 model are close to the solution of the Boltzmann equation when the Knudsen number is less than unity. Figure 12(b) illustrates how the maximum velocity varies against Knudsen number. The NSF equations with the first-order boundary condition are only able to follow the Boltzmann solution when $Kn < 0.1$, i.e. in the slip regime, whilst the R26 equations are in good agreement with the Boltzmann equation up to $Kn \approx 4.0$. The maximum velocity predicted by the NSF equations with the second-order boundary condition and the R13 equations follows the Boltzmann solution up to $Kn \approx 0.4$. Above this value, it increases dramatically due to the overprediction of the slip velocity.

The accurate prediction of the flow rate in a micro-channel is important in the design of micro-devices. To get the flow rate correct, it is essential that the predicted velocity profile is correct. In contrast, the correct prediction of the flow rate cannot guarantee the correct velocity profile. Figure 12 clearly demonstrates that in the transition regime, non-equilibrium effects are no longer confined to the near wall and increasingly enter into the core flow region. Simply using a second-order slip boundary condition (Maurer *et al.* 2003) with a modified accommodation coefficient

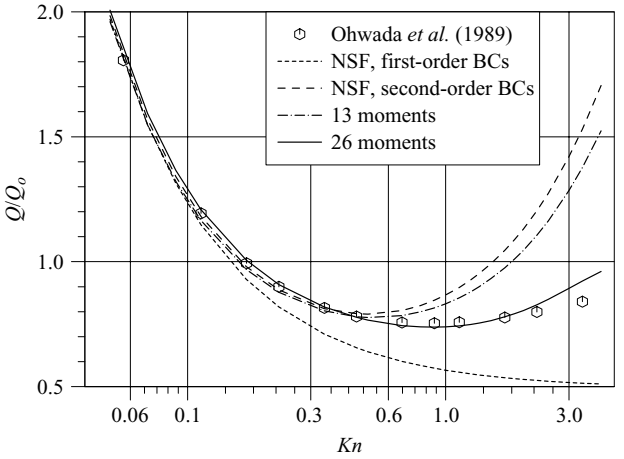

FIGURE 13. Predicted mass flow rate against Knudsen number for pressure-driven Poiseuille flow: symbol, Boltzmann equation solution (Ohwada *et al.* 1989); ——, R26; —·—·, R13; - - - - -, NSF (first-order BCs); – – – – –, NSF (second-order BCs).

will not enhance the predictive capability of the NSF equations in the transition regime. Figure 13 shows the predicted mass flow rates by the NSF, R13 and R26 equations in comparison to the solution obtained from the Boltzmann equation by Ohwada *et al.* (1989). When $Kn < 0.1$ in the slip regime, the flow rates predicted by all models are close to the solution obtained from the Boltzmann equation. As the value of Kn increases, however, non-equilibrium effects gradually enter the central flow region, and the NSF equations with the first-order boundary condition begin to underpredict the mass flow rate, whilst the R26 equations follow the solution obtained from the Boltzmann equation reasonably well until Kn reaches about 2.0. As shown in figure 13, the R26 equations predict a Knudsen minimum at the value of Kn predicted by the Boltzmann equation. The mass flow rate from the NSF equations with a second-order boundary condition and the R13 equations are close to the Boltzmann solution up to $Kn \approx 0.4$. They can also predict a Knudsen minimum but at a value of Kn smaller than that observed by the Boltzmann equation. The Knudsen minimum is the combination of two opposite effects from the rarefaction of the flow interacting in the centre and near the walls, as indicated in figure 12. As the Knudsen number increases, and before it reaches some critical value, the rate of decrease of the maximum velocity in the centre is greater than the rate of increase of the velocity slip. The net result is a reduction in the non-dimensionalized flow rate. As the Knudsen number exceeds this critical value, the increasing contribution of the velocity slip dominates and causes the total flow rate to increase. This is more clearly observed in figure 14 in which the contributions to the total mass flow rate arising from the equilibrium flow component Q^*, the Knudsen layer Q_{Klayer} and velocity slip Q_{slip} are presented for the R26 equations. At $Kn = 0.1$, approximately 50 % of the flow rate is from the bulk flow, and the non-equilibrium contribution of the Knudsen layer is ~ 10 % with wall effects making up the difference. As the Knudsen number increases, the percentage of equilibrium flow decreases dramatically. At $Kn = 0.5$, less than 20 % of the flow is from the bulk flow contribution, whereas the percentage of the flow due to velocity slip increases rapidly with increasing Knudsen number. The contribution from the Knudsen layer to the total flow rate increases up to $Kn = 0.5$

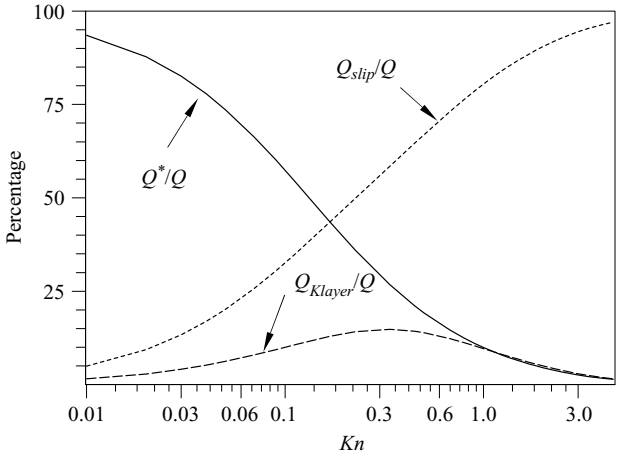

FIGURE 14. Percentages of mass flow rate contribution to the total mass flow rate from bulk flow, Knudsen layer and slip velocity.

and then gradually decreases. For Poiseuille flow, the maximum contribution from the Knudsen layer to the mass flow rate never exceeds 20 %.

6.3. *Rarefied force-driven Poiseuille flow*

When the gas is rarefied, planar force-driven Poiseuille flow exhibits anomalous features, such as a non-constant pressure profile and a bimodal temperature distribution, with a local minimum lying at the centre of the channel. These features were originally predicted by Tij & Santos (1994) using a perturbative solution to the Bhatnagar–Gross–Krook (BGK) model and further confirmed by Mansour, Baras & Garcia (1997) using DSMC. These phenomena were subsequently investigated by Tij, Sabbane & Santos (1998) and Aoki, Takata & Nakanishi (2002) using kinetic theory. However, both the NSF and Burnett equations are unable to capture the observed bimodal temperature profile, even in the slip regime, although the Burnett equations do recover the non-constant pressure profile (Uribe & Garcia 1999). It is recognized that the bimodal effect is of super-Burnett order, and only a theory comparable to this order will be able to capture such a phenomena. Recently, Struchtrup & Torrilhon (2008) predicted the dip of the temperature profile with the linearized R13 equations, which are of third-order accuracy. In the present study, the 10 and the 20 mean free path cases of Mansour *et al.* (1997) are studied with both the full R13 and R26 equations, and the computed results are compared with DSMC data (Uribe & Garcia 1999). More recently, Xu, Liu & Jiang (2007) captured the bimodal temperature profile using a multiple-temperature kinetic model and a first-order expansion to the Navier–Stokes order.

To facilitate the comparison with DSMC data, the gas has the same properties as those specified by Mansour *et al.* (1997), i.e. $m = d = T_R = 1$ and $k = 1/2$, where m is the molecular weight in kilograms; d is the molecular diameter in metres; T_R is the reference temperature in Kelvin; and k is the Boltzmann constant, with the gas constant $R = k/m$. The DSMC data were for a hard sphere gas with a number density of 1.21×10^{-3}, which yields a mean free path $\lambda = 186$ m. For the case of $H = 10\lambda$, the acceleration is $a_x = 1.6 \times 10^{-4}(2kT_R/md)$ and $Kn = 0.1$. For the second case, $H = 20\lambda$ and $a_x = 4.0 \times 10^{-5}(2kT_R/md)$, with $Kn = 0.05$ (Uribe & Garcia 1999).

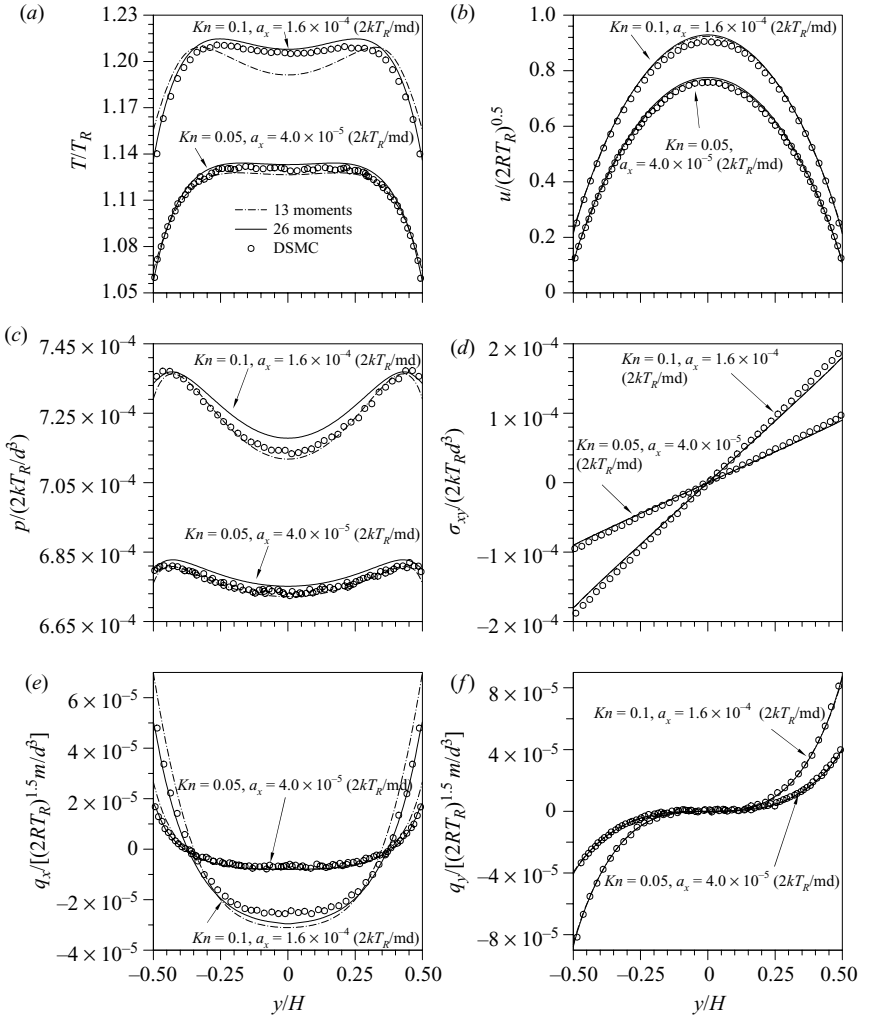

FIGURE 15. Predicted characteristics of force-driven Poiseuille flow: ○, DSMC data (Uribe & Garcia 1999); ——, R26; —·—·—, R13. (*a*) Temperature; (*b*) velocity; (*c*) pressure; (*d*) shear stress; (*e*) tangential heat flux; and (*f*) normal heat flux.

The essential characteristics of force-driven Poiseuille flow are shown in figure 15. Both the R13 and R26 equations are able to reproduce the anomalous features predicted in the DSMC simulations (Uribe & Garcia 1999), such as the bimodal temperature profile, non-constant pressure profile and non-gradient heat flux, fairly accurately. In comparison to the DSMC data, the temperature at the centre of the channel is underpredicted by the R13 equations and slightly overpredicted by the R26 equations. As discussed by Struchtrup & Torrilhon (2008), the characteristic dip is caused by the competition between the positive hydrodynamic term and the negative higher-order correction from higher moments. The temperature shown in figure 15(*a*) includes energy components in the three spatial dimensions. A separate temperature field in each individual direction can also be defined (Bird 1994). For

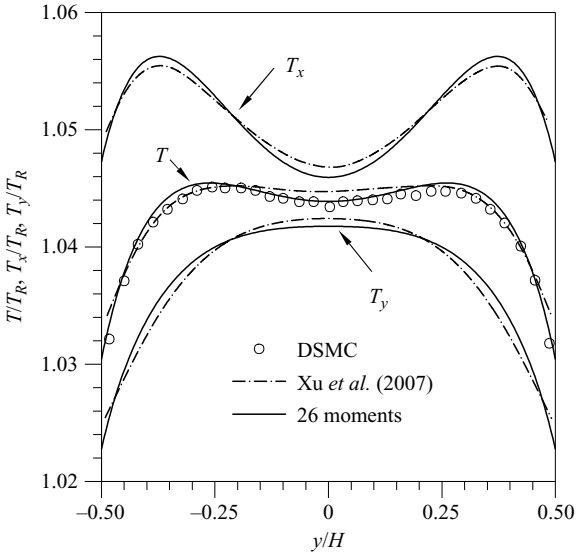

FIGURE 16. Multiple-temperature profiles in force-driven Poiseuille flow: ○, DSMC data (Zheng *et al.* 2002); ——, R26; —·—·, multiple-temperature model (Xu *et al.* 2007).

example temperatures T_x and T_y in the x- and y-direction, respectively, are defined by

$$\rho\frac{k}{m}T_x = \int c_x^2 f \,\mathrm{d}\boldsymbol{\xi} \quad \text{and} \quad \rho\frac{k}{m}T_y = \int c_y^2 f \,\mathrm{d}\boldsymbol{\xi}. \tag{73}$$

From the definitions in (73), it is straightforward to obtain the following relationships:

$$T_x = T + \frac{\sigma_{xx}}{\rho R} \quad \text{and} \quad T_y = T + \frac{\sigma_{yy}}{\rho R}. \tag{74}$$

The computed multiple temperature profiles from the R26 equations are shown in figure 16 along with the results from the multiple-temperature model (Xu *et al.* 2007) for the 10 mean free path case with $a_x = 6.868 \times 10^{-5}(2kT_R/md)$ (Zheng, Garcia & Alder 2002). The values of the temperature in different directions from the moment equations and the multiple-temperature model are in close agreement with each other, which indicates that the multiple-temperature concept is well embedded in the R26 equations.

6.4. *Gradient transport mechanism versus non-gradient transport mechanism*

The GTM predominates in the continuum limit for the macroscopic quantities, which is reflected in the NSF equations. As the gas flow departs from a local equilibrium state, the NGTM starts to have an effect on transport processes for all macroscopic quantities. One obvious example is the tangential heat flux q_x in planar Couette flow, as shown in figure 3. As there is no temperature gradient parallel to the wall, q_x is generated solely by the NGTM. Similarly, the anisotropic normal stresses σ_{xx} and σ_{yy}, shown in figure 4, arise only from the NGTM. However, for the normal heat flux q_y and shear stress σ_{xy}, both the GTM and the NGTM coexist in Couette flow. Figure 17 shows values of q_y and its GTM and NGTM components q_y^G and ρh_y, respectively, for planar Couette flow in the slip and transition regimes. At $Kn = 0.025$, in the slip regime, the normal heat flux q_y follows its GTM component q_y^G up to the region close to the wall, and the NGTM contribution to the total transport in the bulk flow region is negligible. In the slip limit and early transition regime, where $Kn = 0.1$ and 0.25,

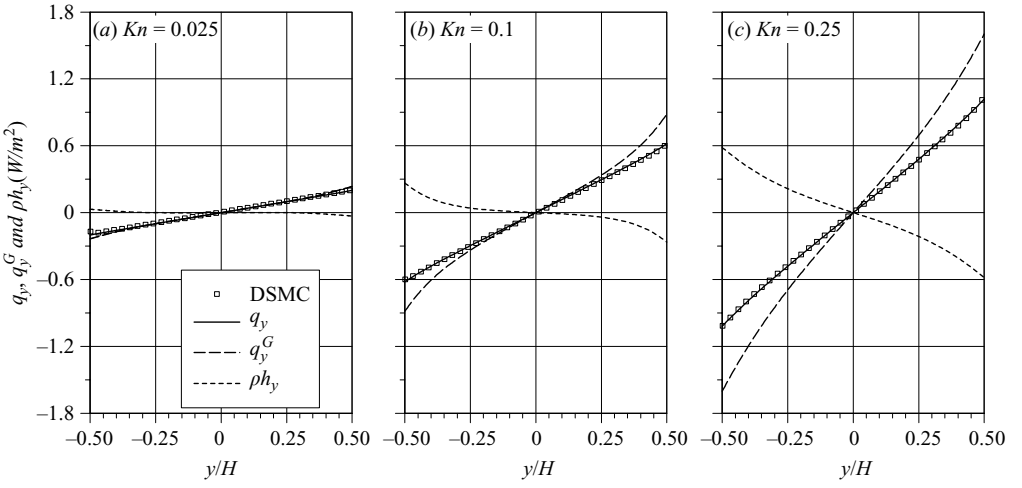

FIGURE 17. Normal heat flux and its GTM and NGMT components of planar Couette flows in slip and transition regimes.

respectively, the GTM and NGTM components have the same order of magnitude throughout the whole region. For planar Couette flow in the transition regime, the temperature profile no longer has a parabolic profile. The normal heat flux calculated according to the GTM q_y^G clearly becomes nonlinear and overestimates the value of the normal heat flux, particularly close to the wall, as demonstrated in figure 17. However, the NGTM ρh_y acts to compensate for the overestimated values of the heat flux. It is therefore necessary to include the higher-order moments to successfully capture any non-gradient transport phenomena in the transition regime.

7. Conclusions

The paper has presented an analysis of the method of moments for low-speed confined flows involving planar Couette flow and pressure- and force-driven Poiseuille flows, and we have successfully extended these models into the transition regime. Limitations were observed in the R13 equations, and a set of regularized 26 moment equations were developed by introducing the third moments into the hydrodynamic system to overcome these problems. The results show that the R13 equations are not able to accurately describe the velocity profile in the Knudsen layers found in planar Couette flow. However, the R26 system can reproduce the Knudsen-layer velocity field and also produce a more accurate description of the shear stress and heat flux in the transition regime. The R13 equations can be used for the Poiseuille flow for a Knudsen number less than 0.4. However, using the R26 equations significantly improves the prediction of both the velocity profile and the mass flow rate up to a Knudsen number of 1.0, and the results are in very good agreement with data obtained from the linearized Boltzmann equation. Above 1.0, the R26 equations start to underpredict the velocity profile at the centre of the channel, but they are able to capture the well-known Knudsen minimum at the correct value of Knudsen number. In addition, the R13 and R26 equations are both able to capture the bimodal temperature profile observed in force-driven Poiseuille flow.

The importance of the GTM and the NGTM has been demonstrated. In addition, the paper has shown it is necessary to include the higher-order moments to successfully capture any non-gradient transport phenomena, particularly in the transition regime.

Currently, there is no precise way to determine the penetration depth of the Knudsen layer. However, it is generally accepted that the layer extends to a distance of $\sim 1.5\lambda$. For a confined-flow problem, we would therefore expect these wall layers to overlap when the channel height is around 3λ, i.e. when $Kn \sim 0.33$. The results from the R26 equations are in good agreement with this intuitive hypothesis.

The paper has benefited from discussions with Professor S. Stefanov (Bulgarian Academy of Science), Professor Jason Reese (University of Strathclyde, Glasgow, UK), Dr H. Struchtrup (University of Victoria, BC, Canada), Dr M. Torrilhon (ETH, Zurich), Dr R. W. Barber, Dr G. H. Tang and Dr S. Mizzi (STFC Daresbury Laboratory, UK) and Dr Y. H. Zhang (University of Strathclyde). The authors would like to thank the Engineering and Physical Sciences Research Council (EPSRC) for their support of Collaborative Computational Project 12 (CCP12).

Appendix A. Derivation of approximations for ϕ_{ijkl}, ψ_{ijk} and Ω_i

To allow some of the higher moments outside the GMM to approach the GMM at a finite fast rate for the 26 moment system, the approximations for ϕ_{ijkl}, ψ_{ijk} and Ω_i are required in § 2. For the rest of the higher moments outside of the GMM for the 26 moment system, it is assumed that they approach the GMM instantly so that they can be calculated with f_{G26}. From the general governing equation for moments (Struchtrup 2005), the governing equations for ϕ_{ijkl}, ψ_{ijk} and Ω_i are

$$\frac{\partial \phi_{ijkl}}{\partial t} + \frac{\partial u_m \phi_{ijkl}}{\partial x_m} + \frac{4}{9}\frac{\partial \psi_{\langle ijk}}{\partial x_{l\rangle}} - 4\frac{m_{\langle ijk}}{\rho}\left(\frac{\partial \sigma_{l\rangle m}}{\partial x_m} + \frac{\partial p}{\partial x_{l\rangle}}\right) + 4RT\frac{\partial m_{\langle ijk}}{\partial x_{l\rangle}} + 4m_{\langle ijk}\frac{\partial RT}{\partial x_{l\rangle}} + 4\phi_{m\langle ijk}\frac{\partial u_{l\rangle}}{\partial x_m} + \frac{12}{7}(R_{\langle ij} + 7RT\sigma_{\langle ij})\frac{\partial u_k}{\partial x_{l\rangle}} = -C_1\frac{p}{\mu}\phi_{ijkl} - C_2\frac{p}{\mu}\frac{\sigma_{\langle ij}\sigma_{kl\rangle}}{\rho}, \tag{A 1}$$

$$\frac{\partial \psi_{ijk}}{\partial t} + \frac{\partial \psi_{ijk}u_m}{\partial x_m} + \frac{27}{7}RT\frac{\partial R_{\langle ij}}{\partial x_{k\rangle}} + \frac{108}{5}RTq_{\langle i}\frac{\partial u_j}{\partial x_{k\rangle}} + \frac{27}{7}(2R_{\langle ij} + 7RT\sigma_{\langle ij})\frac{\partial RT}{\partial x_{k\rangle}} + 8RTm_{\langle ijk}\frac{\partial u_{m\rangle}}{\partial x_m} + \frac{54}{7}RTm_{m\langle ij}\frac{\partial u_m}{\partial x_{k\rangle}} - 6m_{ijk}RT\frac{\partial u_m}{\partial x_m} - 6\frac{m_{ijk}}{\rho}\left(\frac{\partial q_m}{\partial x_m} + \sigma_{ml}\frac{\partial u_m}{\partial x_l}\right) - \frac{27}{7}\frac{R_{\langle ij}}{\rho}\left(\frac{\partial \sigma_{k\rangle m}}{\partial x_m} + \frac{\partial p}{\partial x_{k\rangle}}\right) + \frac{8}{9}\psi_{\langle ijk}\frac{\partial u_{m\rangle}}{\partial x_m} + 3\psi_{m\langle ij}\frac{\partial u_{k\rangle}}{\partial x_m} + \frac{6}{7}\psi_{m\langle ij}\frac{\partial u_m}{\partial x_{k\rangle}} + \frac{54}{35}\Omega_{\langle i}\frac{\partial u_j}{\partial x_{k\rangle}} - 9RT\frac{\partial \phi_{ijkl}}{\partial x_l} - 2\frac{\phi_{ijkm}}{\rho}\left(\frac{\partial \sigma_{ml}}{\partial x_l} + \frac{\partial p}{\partial x_m}\right) = -Y_1\frac{p}{\mu}\psi_{ijk} - \frac{p}{\mu}\left(Y_2\frac{\sigma_{\langle li}m_{jkl\rangle}}{\rho} + Y_3\frac{q_{\langle i}\sigma_{jk\rangle}}{\rho}\right), \tag{A 2}$$

$$\frac{\partial \Omega_i}{\partial t} + \frac{\partial \Omega_i u_j}{\partial x_j} + \frac{7}{3}RT\frac{\partial \Delta}{\partial x_i} + 4RT\frac{\partial R_{ij}}{\partial x_j} - \frac{56}{3}\frac{q_i}{\rho}\left(\frac{\partial q_j}{\partial x_j} + \sigma_{jk}\frac{\partial u_j}{\partial x_k}\right) - 4\frac{R_{ij}}{\rho}\left(\frac{\partial p}{\partial x_j} + \frac{\partial \sigma_{jk}}{\partial x_k}\right) + 7\Delta\frac{\partial RT}{\partial x_i} - \frac{7}{3}\frac{\Delta}{\rho}\left(\frac{\partial p}{\partial x_i} + \frac{\partial \sigma_{ij}}{\partial x_j}\right) + 2(9R_{ij} + 14RT\sigma_{ij})\frac{\partial RT}{\partial x_j} + \frac{56}{5}RT\left(q_j\frac{\partial u_i}{\partial x_j} + q_j\frac{\partial u_j}{\partial x_i}\right) + 4\psi_{ijk}\frac{\partial u_j}{\partial x_k} + 8RTm_{ijk}\frac{\partial u_j}{\partial x_k} + \left(\frac{5}{4}\Omega_i\frac{\partial u_j}{\partial x_j} + \frac{9}{5}\Omega_j\frac{\partial u_i}{\partial x_j} + \frac{4}{5}\Omega_j\frac{\partial u_j}{\partial x_i}\right) = -\frac{p}{\mu}\Omega_i - \frac{2}{15}\frac{p}{\mu}\left(\frac{5m_{ijk}\sigma_{jk} + 14q_j\sigma_{ij}}{\rho}\right). \tag{A 3}$$

The collision production terms on the right are for Maxwell molecules (Truesdell & Muncaster 1980), in which $C_1 = 2.097$, $C_2 = 0.291$, $Y_1 = 1.698$, $Y_2 = 1.203$ and $Y_3 = 0.854$ are collision constants. Whilst the moments in the GMM relax at a time scale of order τ towards the equilibrium state, the higher moments outside the GMM are assumed to change at a time scale order of $\varepsilon\tau$ ($\varepsilon < 1$) towards the GMM and then follow the GMM to relax to the equilibrium state. However, it should be emphasized that the higher moments outside the GMM do not relax at the time scale $\varepsilon\tau$ directly towards the equilibrium state. In other words, the expanded distribution function $f^M(1 + \{\text{GMM}\} + \{\text{terms outside the GMM}\})$ approaches $f^M(1 + \{\text{GMM}\})$ at a rate of $\varepsilon\tau$, whilst $f^M(1 + \{\text{GMM}\})$ relaxes to f^M at a time scale of order τ. As ε is a small parameter, the overall relaxation time towards the equilibrium state for the moments both inside and outside the GMM is of the same order. The relaxation of $f^M(1 + \{\text{GMM}\})$ towards f^M is governed by the moment equations, and the relaxation of $f^M(1 + \{\text{GMM}\} + \{\text{terms outside the GMM}\})$ towards $f^M(1 + \{\text{GMM}\})$ is obtained through the following expansion. With the above assumptions and following the procedure of Struchtrup & Torrilhon (2003), (A 1)–(A 3) can be written as

$$\frac{\partial \phi_{ijkl}}{\partial t} + \{\ldots \text{space derivatives of moments} \ldots\} = -\frac{1}{\varepsilon} C_1 \frac{p}{\mu} \phi_{ijkl} - C_2 \frac{p}{\mu} \frac{\sigma_{\langle ij} \sigma_{kl \rangle}}{\rho}, \tag{A 4}$$

$$\frac{\partial \psi_{ijk}}{\partial t} + \{\ldots \text{space derivatives of moments} \ldots\} = -\frac{1}{\varepsilon} Y_1 \frac{p}{\mu} \psi_{ijk} - \frac{p}{\mu} \times \left(Y_2 \frac{\sigma_{\langle li} m_{jkl \rangle}}{\rho} + Y_3 \frac{q_{\langle i} \sigma_{jk \rangle}}{\rho} \right), \tag{A 5}$$

$$\frac{\partial \Omega_i}{\partial t} + \{\ldots \text{space derivatives of moments} \ldots\} = -\frac{1}{\varepsilon} \frac{p}{\mu} \Omega_i - \frac{2}{15} \frac{p}{\mu} \left(\frac{5 m_{ijk} \sigma_{jk} + 14 q_j \sigma_{ij}}{\rho} \right). \tag{A 6}$$

Equations (A 4)–(A 6) are expanded in terms of the small parameter ε as

$$\left.\begin{aligned} \phi_{ijkl} &= \phi_{ijkl}^{(0)} + \varepsilon \phi_{ijkl}^{(1)} + \varepsilon^2 \phi_{ijkl}^{(2)} + \cdots, \\ \psi_{ijk} &= \psi_{ijk}^{(0)} + \varepsilon \psi_{ijk}^{(1)} + \varepsilon^2 \psi_{ijk}^{(2)} + \cdots, \\ \Omega_i &= \Omega_i^{(0)} + \varepsilon \Omega_i^{(1)} + \varepsilon^2 \Omega_i^{(2)} + \cdots. \end{aligned}\right\} \tag{A 7}$$

Inserting (A 7) into (A 4)–(A 6), we obtain the zeroth-order approximations of ϕ_{ijkl} ψ_{ijk} and Ω_i,

$$\phi_{ijkl}^{(0)} = 0, \ \psi_{ijk}^{(0)} = 0 \text{ and } \Omega_i^{(0)} = 0, \tag{A 8}$$

and their first-order approximations:

$$\phi_{ijkl}^{(1)} = -\frac{4\mu}{C_1} \frac{\partial (m_{\langle ijk}/\rho)}{\partial x_{l \rangle}} - \frac{12}{C_1} \frac{\mu}{\rho} \sigma_{\langle ij} \frac{\partial u_k}{\partial x_{l \rangle}} + \frac{4\mu}{C_1 p \rho} m_{\langle ijk} \frac{\partial \sigma_{l \rangle m}}{\partial x_m} - \frac{12}{7} \frac{\mu R_{\langle ij}}{C_1 p} \frac{\partial u_k}{\partial x_{l \rangle}} - \frac{C_2}{C_1} \frac{\sigma_{\langle ij} \sigma_{kl \rangle}}{\rho}, \tag{A 9a}$$

$$\psi_{ijk}^{(1)} = -\frac{27}{7}\frac{\mu}{Y_1}\frac{\partial(R_{\langle ij}/\rho)}{\partial x_{k\rangle}} - 27\frac{\mu}{Y_1\rho}\sigma_{\langle ij}\frac{\partial RT}{\partial x_{k\rangle}} - \frac{108}{5}\frac{\mu}{Y_1\rho}q_{\langle i}\frac{\partial u_j}{\partial x_{k\rangle}} + \frac{27}{7}\frac{\mu}{Y_1 p}\frac{R_{\langle ij}}{\rho}\frac{\partial \sigma_{k\rangle m}}{\partial x_m}$$
$$-\frac{27}{7}\frac{\mu R_{\langle ij}}{Y_1 p}\frac{\partial RT}{\partial x_{k\rangle}} - \frac{\mu}{Y_1\rho}\left(\frac{54}{7}m_{m\langle ij}\frac{\partial u_m}{\partial x_{k\rangle}} + 8m_{\langle ijk}\frac{\partial u_{m\rangle}}{\partial x_m} - 6m_{ijk}\frac{\partial u_m}{\partial x_m}\right)$$
$$+6\frac{\mu}{Y_1 p}\frac{m_{ijk}}{\rho}\left(\frac{\partial q_m}{\partial x_m} + \sigma_{ml}\frac{\partial u_m}{\partial x_l}\right) - \left(\frac{Y_2}{Y_1}\frac{\sigma_{\langle li}m_{jkl\rangle}}{\rho} + \frac{Y_3}{Y_1}\frac{q_{\langle i}\sigma_{jk\rangle}}{\rho}\right), \tag{A 9b}$$

$$\Omega_i^{(1)} = -\frac{7}{3}\mu\frac{\partial(\Delta/\rho)}{\partial x_i} - \frac{14}{3}\frac{\mu}{p}\Delta\frac{\partial RT}{\partial x_i} - \frac{56}{5}\frac{\mu}{\rho}\left(q_j\frac{\partial u_i}{\partial x_j} + q_j\frac{\partial u_j}{\partial x_i}\right) - 28\frac{\mu}{\rho}\sigma_{ij}\frac{\partial RT}{\partial x_j}$$
$$-18\frac{\mu}{p}R_{ij}\frac{\partial RT}{\partial x_j} - 4\frac{\mu}{\rho}\frac{\partial R_{ij}}{\partial x_j} + \frac{56}{3}\frac{\mu}{p}\frac{q_i}{\rho}\left(\frac{\partial q_j}{\partial x_j} + \sigma_{jk}\frac{\partial u_j}{\partial x_k}\right) + 4\frac{\mu}{p}\frac{R_{ij}}{\rho}\left(\frac{\partial p}{\partial x_j} + \frac{\partial \sigma_{jk}}{\partial x_k}\right)$$
$$+\frac{7}{3}\frac{\Delta}{\rho}\frac{\mu}{p}\frac{\partial \sigma_{ij}}{\partial x_j} - 8\frac{\mu}{\rho}m_{ijk}\frac{\partial u_j}{\partial x_k} - \frac{2}{15}\left(\frac{5m_{ijk}\sigma_{jk} + 14q_j\sigma_{ij}}{\rho}\right). \tag{A 9c}$$

The first-order approximations of the above moments are used to regularize the 26 moment equations and construct the WBCs in § 2 and 3, respectively.

Appendix B. Coefficients for a fifth-order molecular distribution function in Hermite polynomials

Grad (1949*b*) expanded f in Hermite polynomials as

$$f = f_M\sum_{n=0}^{\infty}\frac{1}{n!}a_A^{(n)}H_A^{(n)} = f_M\left(a^{(0)}H^{(0)} + a_i^{(1)}H_i^{(1)} + \frac{1}{2!}a_{ij}^{(2)}H_{ij}^{(2)} + \frac{1}{3!}a_{ijk}^{(3)}H_{ijk}^{(3)} + \cdots\right), \tag{B 1}$$

where $H_A^{(n)}$ is the Hermite function; $a_A^{(n)}$ are the coefficients; and f_M is the local Maxwellian distribution function given by

$$f_M = \frac{\rho}{\sqrt{(2\pi RT)^3}}\exp\left(-\frac{c^2}{2RT}\right).$$

The expressions of the polynomials and their associated coefficients used in the § 3 to derive the fifth-order approximation of the molecular distribution function $f^{(5)}$ are (Grad 1949*a*, *b*)

$$\left.\begin{aligned}
H^{(0)} &= 1,\ H_i^{(1)} = \frac{c_i}{\sqrt{RT}},\ H_{ij}^{(2)} = \frac{c_ic_j}{RT} - \delta_{ij},\ H_{ijk}^{(3)} = \frac{c_ic_jc_k}{RT\sqrt{RT}} - \frac{c_i\delta_{jk} + c_j\delta_{ik} + c_k\delta_{ij}}{\sqrt{RT}},\\
H_{ijkl}^{(4)} &= \frac{c_ic_jc_kc_l}{(RT)^2} - \frac{c_ic_j\delta_{kl} + c_ic_k\delta_{jl} + c_ic_l\delta_{jk} + c_jc_k\delta_{il} + c_jc_l\delta_{ik} + c_kc_l\delta_{ij}}{RT} + D_{ijkl},\\
H_{ijklm}^{(5)} &= \frac{c_ic_jc_kc_lc_m}{RT^2\sqrt{RT}} - \frac{c_ic_jc_m\delta_{kl} + c_ic_kc_m\delta_{jl} + c_ic_lc_m\delta_{jk} + c_jc_kc_m\delta_{il} + c_jc_lc_m\delta_{ik} + c_kc_lc_m\delta_{ij}}{RT\sqrt{RT}}\\
&\quad - \frac{c_lc_jc_k\delta_{im} + c_lc_ic_k\delta_{jm} + c_ic_jc_l\delta_{km} + c_ic_jc_k\delta_{lm}}{RT\sqrt{RT}}\\
&\quad + \frac{c_iD_{jklm} + c_jD_{iklm} + c_kD_{ijlm} + c_lD_{ijkm} + c_mD_{ijkl}}{\sqrt{RT}}
\end{aligned}\right\} \tag{B 2}$$

and

$$\left.\begin{aligned}
a^{(0)} &= 1,\ a_i^{(1)} = 0,\ a_{ij}^{(2)} = \frac{\sigma_{ij}}{p},\ a_{ijk}^{(3)} = \frac{m_{ijk}}{p\sqrt{RT}} + \frac{2}{5}\frac{(q_i\,\delta_{jk} + q_j\,\delta_{ik} + q_k\,\delta_{ij})}{p\sqrt{RT}},\\
a_{ijkl}^{(4)} &= \frac{\phi_{ijkl}}{pRT} + \frac{R_{ij}\delta_{kl} + R_{ik}\delta_{jl} + R_{il}\delta_{jk} + R_{jk}\delta_{il} + R_{jl}\delta_{ik} + R_{kl}\delta_{ij}}{7pRT} + \frac{\Delta}{15pRT}D_{ijkl},\\
a_{ijklm}^{(5)} &= \frac{1}{9pRT\sqrt{RT}}(\psi_{ijm}\delta_{kl} + \psi_{ikm}\delta_{jl} + \psi_{ilm}\delta_{jk} + \psi_{jkm}\delta_{il} + \psi_{jlm}\delta_{ik} + \psi_{klm}\delta_{ij}\\
&\quad + \psi_{ijk}\delta_{lm} + \psi_{ijl}\delta_{km} + \psi_{ikl}\delta_{jm} + \psi_{jkl}\delta_{im})\\
&\quad + \frac{\Omega_i D_{jklm} + \Omega_j D_{iklm} + \Omega_k D_{ijlm} + \Omega_l D_{ijkm} + \Omega_m D_{ijkl}}{35pRT\sqrt{RT}},
\end{aligned}\right\} \tag{B 3}$$

where $D_{ijkl} = \delta_{ij}\delta_{kl} + \delta_{ik}\delta_{jl} + \delta_{il}\delta_{jk}$.

Appendix C. WBCs for the R26 equations

The remaining WBCs for the R26 equations obtained in § 3 are listed below:

$$\sigma_{\tau\tau} = -\frac{2-\alpha}{\alpha}\sqrt{\frac{\pi RT}{2}}\left(\frac{5m_{n\tau\tau}+2q_n}{5RT}\right) + p_\alpha\left(\hat{u}_\tau^2+\hat{T}_w-1\right) - \frac{R_{\tau\tau}+R_{nn}}{14RT} - \frac{\Delta}{30RT} - \frac{\phi_{nn\tau\tau}}{2RT}, \tag{C 1}$$

$$\sigma_{nn} = -\frac{2-\alpha}{\alpha}\sqrt{\frac{\pi RT}{2}}\left(\frac{5m_{nnn}+6q_n}{10RT}\right) + p_\alpha(\hat{T}_w-1) - \frac{R_{nn}}{7RT} - \frac{\Delta}{30RT} - \frac{\phi_{nnnn}}{6RT}, \tag{C 2}$$

$$\begin{aligned}
q_\tau &= -\frac{5}{18}\frac{2-\alpha}{\alpha}\sqrt{\frac{\pi RT}{2}}\left(7\sigma_{n\tau}+\frac{R_{n\tau}}{RT}\right) - \frac{5\hat{u}_\tau p_\alpha\sqrt{RT}\left(\hat{u}_\tau^2+6\hat{T}_w\right)}{18} - \frac{10m_{nn\tau}}{9} - \frac{5\psi_{nn\tau}}{81RT}\\
&\quad - \frac{\Omega_\tau}{56RT},
\end{aligned} \tag{C 3}$$

$$\begin{aligned}
m_{\tau\tau\tau} &= -\frac{2-\alpha}{\alpha}\sqrt{\frac{\pi RT}{2}}\left(3\sigma_{n\tau} + \frac{3R_{n\tau}}{7RT} + \frac{\phi_{n\tau\tau\tau}}{RT}\right) - p_\alpha\hat{u}_\tau\sqrt{RT}\left(\hat{u}_\tau^2+3\hat{T}_w\right) - \frac{3m_{nn\tau}}{2}\\
&\quad - \frac{9q_\tau}{5} - \frac{9\Omega_\tau}{280RT} - \frac{2\psi_{\tau\tau\tau}+3\psi_{nn\tau}}{36RT},
\end{aligned} \tag{C 4}$$

$$m_{nn\tau} = -\frac{2-\alpha}{\alpha}\sqrt{\frac{\pi RT}{2}}\left(\sigma_{\tau n}+\frac{R_{n\tau}}{7RT}+\frac{\phi_{nnn\tau}}{3RT}\right) - \frac{2}{5}q_\tau - \frac{2\hat{T}_w\hat{u}_\tau p_\alpha\sqrt{RT}}{3} - \frac{\psi_{nn\tau}}{18RT} - \frac{\Omega_\tau}{140RT}, \tag{C 5}$$

$$\begin{aligned}
R_{\tau\tau} &= -\frac{2-\alpha}{\alpha}\sqrt{\frac{\pi RT}{2}}\left(\frac{28q_n}{15} + \frac{14m_{n\tau\tau}}{3} + \frac{\Omega_n}{15RT} + \frac{14\psi_{n\tau\tau}}{27RT}\right)\\
&\quad + \frac{7p_\alpha RT\left(\hat{u}_\tau^4+6\hat{T}_w\hat{u}_\tau^2+3\hat{T}_w^2-3\right)}{9} - \frac{14RT\sigma_{\tau\tau}}{3} - \frac{R_{nn}}{3} - \frac{14\Delta}{45} - \frac{7(\phi_{\tau\tau\tau\tau}+3\phi_{nn\tau\tau})}{9},
\end{aligned} \tag{C 6}$$

$$\begin{aligned}
R_{nn} &= -\frac{2-\alpha}{\alpha}\sqrt{\frac{\pi RT}{2}}\left(\frac{21q_n}{8} + \frac{35m_{nnn}}{16} + \frac{35\psi_{nnn}}{144RT} + \frac{3\Omega_n}{32RT}\right) + \frac{7p_\alpha RT\left(\hat{T}_w^2-1\right)}{4}\\
&\quad - \frac{7RT\sigma_{nn}}{2} - \frac{7\Delta}{30} - \frac{7\phi_{nnnn}}{6}
\end{aligned} \tag{C 7}$$

and

$$\Delta = -\frac{35}{4}\frac{2-\alpha}{\alpha}\sqrt{\frac{\pi RT}{2}}\left(q_n + \frac{\Omega_n}{28RT}\right) - \frac{5}{4}p_\alpha RT\left(6 - 6\hat{T}_w^2 - \frac{\hat{u}_\tau^4}{4} - 3\hat{u}_\tau^2\hat{T}_w\right) - \frac{15}{4}RT\sigma_{nn} - \frac{15}{8}R_{nn} + \frac{35}{48}\phi_{nnnn}. \quad \text{(C 8)}$$

Here $\sigma_{\tau\tau}$, σ_{nn}, $\sigma_{\tau n}$, q_τ, q_n, $m_{\tau\tau\tau}$, $m_{n\tau\tau}$, $m_{nn\tau}$, m_{nnn}, $R_{\tau\tau}$, $R_{n\tau}$ and R_{nn} are the tangential and normal components of σ_{ij}, q_i, m_{ijk}, R_{ij} relative to the wall. The values of g_{ij}, h_i, $\omega_{ijk}\gamma_{ij}$ and χ at the wall can be calculated from the above list.

REFERENCES

Alves, M. A., Oliveira, P. J. & Pinho, F. T. 2003 A convergent and universally bounded interpolation scheme for the treatment of advection. *Intl J. Numer. Meth. Fluids* **41**, 47–75.

Aoki, K., Takata, S. & Nakanishi, T. 2002 Poiseuille-type flow of a rarefied gas between two parallel plates driven by a uniform external force. *Phys. Rev.* E **65**, 026315.

Aoki, K., Yoshida, H., Nakanishi, T. & Garcia, A. L. 2003 Inverted velocity profile in the cylindrical Couette flow of a rarefied gas. *Phys. Rev.* E **68**, 016302.

Baker, L. L. & Hadjiconstantinou, N. G. 2005 Variance reduction for Monte Carlo solutions of the Boltzmann equation. *Phys. Fluids* **17**, 051703.

Bird, G. 1994 *Molecular Gasdynamics and the Direct Simulation of Gas Flows.* Clarendon.

Bobylev, A. V. 1982 The Chapman–Enskog and Grad method for solving the Boltzmann equation. *Sov. Phys.-Dokl.* **27**, 29–31.

Cercignani, C. 1988 *The Boltzmann Equation and Its Applications.* Springer.

Cercignani, C. 2000 *Rarefied Gasdynamics: From Basic Concepts to Actual Calculations.* Cambridge University Press.

Chapman, S. & Cowling, T. G. 1970 *The Mathematical Theory of Non-uniform Gases.* Cambridge University Press.

Chen, S. & Doolen, G. D. 1998 Lattice Boltzmann method for fluid flows. *Annu. Rev. Fluid Mech.* **30**, 329–364.

Chikatamarla, S. S., Ansumali, S. & Karlin, I. V. 2006 Grad's approximation for missing data in lattice Boltzmann simulations. *Europhys. Lett.* **74**, 215–221.

Debnath, L. 1997 *Nonlinear Partial Differential Equations for Scientists and Engineers.* Birkhauser.

Ferziger, J. H. & Peric, M. 1999 *Computational Methods for Fluid Dynamics*, 2nd edn. Springer.

Gad-El-Hak, M. 1999 The fluid mechanics of microdevices – the Freeman scholar lecture. *J. Fluids Engng* **121**, 5–33.

García-Colín, L. S., Velaso, R. M. & Uribe, F. J. 2008 Beyond the Navier–Stokes equations: Burnett hydrodynamics. *Phys. Rep.* **465**, 149–189.

Gaskell, P. H. & Lau, A. K. C. 1988 Curvature-compensated convective transport: SMART, a new boundedness-preserving transport algorithm. *Intl J. Numer. Meth. Fluids* **8**, 617–641.

Grad, H. 1949*a* Note on N-dimensional Hermite polynomials. *Comm. Pure Appl. Math.* **2**, 325–330.

Grad, H. 1949*b* On the kinetic theory of rarefied gases. *Comm. Pure Appl. Math.* **2**, 331–407.

Grad, H. 1952 The profile of steady plane shock wave. *Comm. Pure Appl. Math.* **5**, 257–300.

Grad, H. 1963 Asymptotic theory of the Boltzmann equation. *Phys. Fluids* **6**, 147–181.

Gorban, A. N., Karlin, I. V. & Zinovyev, A. Y. 2004 Constructive methods of invariant manifolds for kinetic problems. *Phys. Rep.* **396**, 197–403.

Gu, X. J., Barber, R. W. & Emerson, D. R. 2007 How far can 13 moments go in modelling microscale gas phenomena? *Nanoscale Microscale Thermophys. Engng* **11**, 85–97.

Gu, X. J. & Emerson, D. R. 2007 A computational strategy for the regularized 13 moment equations with enhanced wall-boundary conditions. *J. Comput. Phys.* **225**, 263–283.

Guénette, R. & Fortin, M. 1995 A new mixed finite element method for computing viscoelastic flows. *J. Non-Newton. Fluid Mech.* **60**, 27–52.

Hadjiconstantinou, N. G. 2005 Oscillatory shear-driven gas flows in the transition and free-molecular-flow regimes, *Phys. Fluids* **17**, 100611.

Hadjiconstantinou, N. G. 2006 The limits of Navier–Stokes theory and kinetic extensions for describing small-scale gaseous hydrodynamics. *Phys. Fluids* **18**, 111301.

Harley, J. C., Huang, Y., Bau, H. B. & Zemel, J. N. 1995 Gas flow in micro-channels. *J. Fluid Mech.* **284**, 257–274.

Jin, S., Pareshi, L. & Slemrod, M. 2002 A relaxation scheme for solving the Boltzmann equation based on the Chapman–Enskog expansion. *Acta Math. Appl. Sinica* **18**, 37–62.

Jin, S. & Slemrod, M. 2001 Regularization of the Burnett equations via relaxation. *J. Stat. Phys.* **103**, 1009–1033.

Karlin, I. V. & Gorban, A. N. 2002 Hydrodynamics from Grad's equations: what can we learn from the exact solutions? *Ann. Phys.* **11**, 783–833.

Karlin, I. V., Gorban, A. N., Dukek, G. & Nonnenmacher, T. F. 1998 Dynamic correction to moment approximations. *Phys. Rev.* E **57**, 1668–1672.

Kogan, M. N. 1969 *Rarefied Gas Dynamics*. Plenum.

Leonard, B. P. 1979 A stable and accurate convection modelling procedure based on quadratic upstream interpolation. *Comput. Mech. Appl. Mech. Engng* **19**, 59–98.

Levermore, C. D. 1996 Moment closure hierarchies for kinetic theories. *J. Stat. Phys.* **83**, 1021–1065.

Levermore, C. D., Morokoff, W. J. & Nadiga, B. T. 1998 Moment realizability and the validity of the Navier–Stokes equations for rarefied gasdynamics. *Phys. Fluids* **10**, 3214–3226.

Lilly, C. R. & Sader J. E. 2007 Velocity gradient singularity and structure of the velocity profile in the Knudsen layer according to the Boltzmann equation. *Phys. Rev.* E **76**, 026315.

Lilly, C. R. & Sader J. E. 2008 Velocity profile in the Knudsen layer according to the Boltzmann equation. *Proc. R. Soc.* A **464**, 2015–2035.

Liu, I. S. & Rincon M. A. 2004 A boundary value problem in extended thermodynamics – one-dimensional steady flows with heat conduction. *Contin. Mech. Thermodyn.* **16**, 109–124.

Mansour, M. M., Baras, F. & Garcia, A. L. 1997 On the validity of hydrodynamics in plane Poiseuille flow. *Physica* A **240**, 255–267.

Marques, W. & Kremer, G. M. 2001 Couette flow from a thirteen field theory with slip and jump boundary conditions. *Contin. Mech. Thermodyn.* **13**, 207–217.

Maurer, J., Tabeling, P., Joseph, P. & Willaime, H. 2003 Second-order slip laws in microchannels for helium and nitrogen. *Phys. Fluids* **15**, 2613–2621.

Maxwell, J. C. 1879 On stresses in rarified gases arising from inequalities of temperature. *Phil. Trans. R. Soc. Lond.* **170**, 231–256.

Mizzi, S., Gu, X. J., Emerson, D. R., Barber, R. W. & Reese, J. M. 2008 Computational framework for the regularised 20-moment equations for non-equilibrium gas flows. *Intl J. Numer. Meth. Fluids* **56**, 1433–1439.

Muller, I. & Ruggeri, T. 1993 *Extended Thermodynamics*. Springer.

Ohwada, T., Sone, Y. & Aoki, K. 1989 Numerical analysis of the Poiseuille and thermal transpiration flows between two parallel plates on the basis of the Boltzmann equation for hard-sphere molecules. *Phys. Fluids* A **1**, 2042–2049.

Patankar, S. V. 1980 *Numerical Heat Transfer and Fluid Flow*. McGraw-Hill.

Rajagopalan, D., Armstrong, R. C. & Brown, R. A. 1990 Finite element methods for calculation of steady, viscoelastic flow using constitution equations with a Newtonian viscosity. *J. Non-Newton. Fluid Mech.* **36**, 159–192.

Reese, J. M., Gallis, M. A. & Lockerby, D. A. 2003 New directions in fluid dynamics: non-equilibrium aerodynamic and microsystem flows, *Phil. Trans. R. Soc. Lond.* A **361**, 2967–2988.

Reitebuch, D. & Weiss, W. 1999 Application of high moment theory to the plane Couette flow. *Contin. Mech. Thermodyn.* **11**, 217–225.

Renardy, M. 2000 *Mathematical Analysis of Viscoelastic Flows*. SIAM.

Rhie, C. M. & Chow, W. L. 1983 Numerical study of turbulent flow past an airfoil with trailing edge separation. *AIAA J.* **21**, 1525–1532.

Shan, X., Yuan, X.-F. & Chen, H. 2006 Kinetic theory representation of hydrodynamics: a way beyond the Navier–Stokes equation. *J. Fluid Mech.* **550**, 413–441.

Sharipov, F. 1999 Non-isothermal gas flow through rectangular microchannels. *J. Micromech. Microengng* **9**, 394–401.

Shavaliyev, M. S. 1993 Super-Burnett corrections to the stress tensor and the heat flux in a gas of Maxwellian molecules. *J. Appl. Math. Mech.* **57**, 573–576.

Shen, C., Fan, J. & Xie, C. 2003 Statistical simulation of rarefied gas flows in micro-channels. *J. Comput. Phys.* **189**, 512–526.

Siewert, C. E. 2003 The linearized Boltzmann equation: concise and accurate solutions to basic flow problems. *Zeitsch. Angew. Math. Phys.* **54**, 273–303.

Sone, Y., Takata, S. & Ohwada, T. 1990 Numerical-analysis of the plane Couette-flow of a rarefied-gas on the basis of the linearized Boltzmann-equation for hard-sphere molecules. *Eur. J. Mech.* B **9**, 273–288.

Struchtrup, H. 2003 Grad's moment equations for microscale flows. In *Symposium on Rarefied Gasdynamics 23* (ed. A. D. Kestdever & E. P. Muntz), AIP Conference Proceedings, vol. 663, pp. 792–799.

Struchtrup, H. 2004 Stable transport equations for rarefied gases at higher orders in the Knudsen number. *Phys. Fluids* **16**, 3921–3934.

Struchtrup, H. 2005 *Macroscopic Transport Equations for Rarefied Gas Flows*. Springer.

Struchtrup, H. 2008 Linear kinetic transfer: moment equations, boundary conditions, and Knudsen layer. *Physica* A **387**, 1750–1766.

Struchtrup, H. & Torrihon, M. 2003 Regularization of Grad's 13 moment equations: derivation and linear analysis. *Phys. Fluids* **15**, 2668–2680.

Struchtrup, H. & Torrihon, M. 2007 H Theorem, regularization and boundary conditions for linearized 13 moment equations. *Phys. Rev. Lett.* **99**, 014502.

Struchtrup, H. & Torrihon, M. 2008 Higher order effects in rarefied channel flows. *Phys. Rev.* E **78**, 046301.

Succi, S. 2001 *The Lattice Boltzmann Equation for Fluid Dynamics and Beyond*. Clarendon.

Sun, Q. & Boyd, I. D. 2004 Drag on a flat plate in low-Reynolds-number gas flows. *AIAA J.* **42**, 1066–1072.

Tij, M., Sabbane, M. & Santos, A. 1998 Nonlinear Poiseuille flow in a gas. *Phys. Fluids* **10**, 1021–1027.

Tij, M. & Santos, A. 1994 Perturbation analysis of a stationary nonequilibrium flow generated by an external force. *J. Stat. Phys.* **76**, 1399–1414.

Toro, E. F. 1999 *Riemann Solvers and Numerical Methods for Fluids Dynamics: A Practical Introduction*, 2nd edn. Springer.

Torrilhon, M. 2006 Two-dimensional bulk microflow simulations based on regularised Grad's 13 moment equations. *Multiscale Model. Simul.* **5**, 695–728.

Torrilhon, M. & Struchtrup, H. 2004 Regularized 13 moment equations: shock structure calculations and comparison to Burnett models. *J. Fluid Mech.* **513**, 171–198.

Torrilhon, M. & Struchtrup, H. 2008 Boundary conditions for regularized 13-moment-equations for micro-channel-flows. *J. Comput. Phys.* **227**, 1982–2011.

Truesdell, C. & Muncaster, R. G. 1980 *Fundamentals of Maxwell's Kinetic Theory of a Simple Monotomic Gas*. Academic.

Uribe, F. J. & Garcia, A. L. 1999 Burnett description for plane Poiseuille flow. *Phys. Rev.* E **60**, 4063–4078.

Uribe, F. J., Velasco, R. M. & García-Colín, L. S. 2000 Bobylev's instability, *Phys. Rev.* E **62**, 5835–5838.

White, F. M. 1991 *Viscous Fluid Flow*. McGraw-Hill.

Xu, K. 2001 A gas-kinetic BGK scheme for the Navier–Stokes equations and its connection with artificial dissipation and Godunov method. *J. Comput. Phys.* **171**, 289–335.

Xu, K. & Li, Z. 2004 Microchannel flow in the slip regime: gas-kinetic BGK-Burnett solutions. *J. Fluid Mech.* **513**, 87–110.

Xu, K., Liu, H. & Jiang, J. 2007 Multiple-temperature kinetic model for continuum and near continuum flows. *Phys. Fluids* **19**, 016101.

Zhang, Y.-H., Gu, X. J., Barber, R. W. & Emerson, D. R. 2007 Modelling thermal flow in the transition regime using a lattice Boltzmann approach. *Europhys. Lett.* **77**, 30003.

Zheng, Y., Garcia, A. L. & Alder, B. J. 2002 Comparison of kinetic theory and hydrodynamics for Poiseuille flow. *J. Stat. Phys.* **109**, 495–505.